Monthly Notices
of the
ROYAL ASTRONOMICAL SOCIETY

MNRAS **436,** 1721–1740 (2013)
Advance Access publication 2013 October 3

doi:10.1093/mnras/stt1691

Viscous Kelvin–Helmholtz instabilities in highly ionized plasmas

E. Roediger,[1,2,3]★ R. P. Kraft,[3] P. Nulsen,[3] E. Churazov,[4] W. Forman,[3] M. Brüggen[1] and R. Kokotanekova[2,3,5]

[1]*Hamburger Sternwarte, Universität Hamburg, Gojenbergsweg 112, D-21029 Hamburg, Germany*
[2]*Jacobs University Bremen, PO Box 750 561, D-28725 Bremen, Germany*
[3]*Harvard/Smithsonian Center for Astrophysics, 60 Garden Street, MS-4, Cambridge, MA 02138, USA*
[4]*Max-Planck-Institut für Astrophysik, Karl-Schwarzschild-Strasse 1, D-85741 Garching, Germany*
[5]*AstroMundus Master Programme, University of Innsbruck, Technikerstr. 25/8, 6020 Innsbruck, Austria*

Accepted 2013 September 5. Received 2013 September 3; in original form 2013 July 19

ABSTRACT

Transport coefficients in highly ionized plasmas like the intracluster medium (ICM) are still ill-constrained. They influence various processes, among them the mixing at shear flow interfaces due to the Kelvin–Helmholtz instability (KHI). The observed structure of potential mixing layers can be used to infer the transport coefficients, but the data interpretation requires a detailed knowledge of the long-term evolution of the KHI under different conditions. Here we present the first systematic numerical study of the effect of constant and temperature-dependent isotropic viscosity over the full range of possible values. We show that moderate viscosities slow down the growth of the KHI and reduce the height of the KHI rolls and their rolling-up. Viscosities above a critical value suppress the KHI. The effect can be quantified in terms of the Reynolds number $\mathrm{Re} = U\lambda/\nu$, where U is the shear velocity, λ the perturbation length and ν the kinematic viscosity. We derive the critical Re for constant and temperature-dependent Spitzer-like viscosities, an empirical relation for the viscous KHI growth time as a function of Re and density contrast, and describe special behaviours for Spitzer-like viscosities and high density contrasts. Finally, we briefly discuss several astrophysical situations where the viscous KHI could play a role, i.e. sloshing cold fronts, gas stripping from galaxies, buoyant cavities, ICM turbulence and high-velocity clouds.

Key words: hydrodynamics – instabilities – plasmas – methods: numerical – galaxies: clusters: intracluster medium – X-rays: galaxies: clusters.

1 INTRODUCTION

The classic Kelvin–Helmholtz instability (KHI) arises due to a shear flow parallel to the interface between two inviscid incompressible fluids. The fluids are in pressure equilibrium, but the shear velocity and possibly the density change discontinuously at the interface. Small perturbations at the interface grow exponentially (Lamb 1932; Chandrasekhar 1961; Drazin & Reid 2004), and the distorted interface rolls up into the classic Kelvin–Helmholtz (KH) rolls or cat-eye patterns (see e.g. Fig. 1 later-on). As shear flows are ubiquitous in astrophysical fluids, the KHI is a major agent for turbulence generation and mixing.

Several special conditions or fluid properties can fully or partially suppress the KHI, among them gravity, magnetic fields and viscosity. Thus, if the dynamical conditions at a shear layer are known, the presence or absence of the KHI can in principle be used to constrain the properties of the fluid.

This prospect is particularly interesting for the intracluster medium (ICM) in galaxy clusters and hot haloes of galaxies. At temperatures of up to a few keV, this gas is a highly ionized plasma, and it is weakly magnetized (e.g. Ferrari et al. 2008; Bonafede et al. 2010). Its effective transport properties, i.e. thermal conduction and viscosity, are still ill-constrained. If the ICM was not magnetized, the transport coefficients due to Coulomb collisions would be large (Spitzer 1956). For example, the importance of viscosity can be expressed by the Reynolds number $\mathrm{Re} = UL/\nu$, where U is a characteristic velocity of the gas flow, L a characteristic length scale and ν the kinematic viscosity. The kinematic viscosity in an unmagnetized plasma scales as $\nu \propto T^{5/2}n^{-1}$ (Spitzer 1956; Sarazin 1988), and for typical values of ICM temperature $T_{\rm ICM}$ and electron particle density $n_{\rm e}$ the Reynolds number becomes

$$\mathrm{Re} = 10\, f_\mu^{-1} \left(\frac{U}{400\,\mathrm{km\,s^{-1}}}\right) \left(\frac{L}{10\,\mathrm{kpc}}\right) \left(\frac{n_{\rm e}}{10^{-3}\,\mathrm{cm^{-3}}}\right) \times \left(\frac{kT_{\rm ICM}}{2.4\,\mathrm{keV}}\right)^{-5/2}. \quad (1)$$

★ E-mail: eroediger@hs.uni-hamburg.de

We allowed for a reduced viscosity in equation (1) by including the viscosity suppression factor $f_\mu \leq 1$. In the presence of magnetic fields the particle mean free path perpendicular to the field lines is reduced dramatically, leading to anisotropic transport coefficients. However, tangled magnetic fields could lead to a reduced isotropic *effective* mean free path and transport coefficients on macroscopic scales. Microscale instabilities might have even more dramatic effects on transport in the intracluster plasma (Rosin et al. 2011). Collisionality in the ICM could be mediated by interactions between magnetohydrodynamic waves and the particles. The resulting *effective* transport processes in the ICM could range from reduced isotropic conduction and viscosity (Narayan & Medvedev 2001) to anisotropic transport coefficients (Kunz et al. 2012), and the effective viscosity and thermal conduction may even experience different suppression factors. Isotropic and anisotropic viscosities could affect the KHI differently, e.g. in the latter case the orientation of the magnetic field with respect to the interface may play a role. However, so far the nature of the *effective* viscosity is still unconstrained observationally. Therefore, in this paper we focus on the effect of an isotropic viscosity.

In the ICM, observable shear flows occur in different dynamical contexts. Prominent examples are sloshing cold fronts (CFs), upstream edges and tails of gas-stripped galaxies or merger cores, or the surfaces of buoyantly rising cavities that have been inflated by active galactic nuclei (AGN). The quality of the observational data has become sufficient to show the structure of the shear layers. For example, the cluster Abell 496 (Dupke, White & Bregman 2007; Roediger et al. 2012a) has boxy CFs with kinks and doublets. We identified distorted fronts also in the merging groups around NGC 7619 and UGC 12491 (Roediger et al. 2012b). Several gas-stripped elliptical galaxies falling into their host clusters have been observed deeply. They all show an upstream contact discontinuity and a tail of stripped gas, but their detailed structures differ. The tail of M86 starts in a plume, bends and bifurcates (Randall et al. 2008). In M89 (Machacek et al. 2006) and M49 (Kraft et al. 2011) the upstream edges have a ragged appearance with horns and kinks. In contrast, the upstream edge of NGC 1404 (Machacek et al. 2005) appears to be smooth. Numerous AGN inflated cavities have been observed, despite the fact that in purely hydrodynamical simulations they are disrupted by Rayleigh–Taylor instabilities (RTIs) and KHIs. The presence or absence of substructure at these shear layers indicates the presence or suppression of KHIs.

Several groups started investigating the impact of ICM properties on such shear layers. Reynolds et al. (2005) and Guo et al. (2012) demonstrated that buoyantly rising or even currently inflating cavities can be stabilized by viscosity. Dong & Stone (2009) pointed out that in the case of anisotropic viscosity the evolution of the bubbles depends on the magnetic field orientation because preferentially instabilities parallel to the field lines are suppressed. Lyutikov (2006) and Dursi & Pfrommer (2008) showed that magnetic draping can stabilize the cavities, although Ruszkowski et al. (2007) stressed out that this requires magnetic fields with coherence lengths larger than the cavity size. Magnetic draping can also suppress instabilities at gas-stripped galaxies (Dursi & Pfrommer 2008; Ruszkowski et al. 2012). Viscosity, however, could have a similar effect (Roediger & Brüggen 2008). Sloshing CFs in hydrodynamical simulations are distorted by KHIs, which can be reduced or suppressed by sufficiently aligned magnetic fields (ZuHone, Markevitch & Lee 2011) or viscosity (Roediger et al. 2013).

In all of these situations the KHI occurs in a complex dynamical context. Shear velocities can vary in time and space, the shear layers are curved and experience gravity. In order to provide a solid basis for studies that include these complex dynamical contexts, here we focus on the impact of an isotropic viscosity on the KHI in idealized setups. Already the linear stability analysis of the viscous KHI is complicated (see Section 2), and, to our knowledge, no previous work investigated the long-term evolution of the viscous KHI. Here we do so with a systematic numerical study. In particular, we

(i) show analytically that viscosity suppresses the KHI below a critical Reynolds number;
(ii) investigate not only the onset of the KHI, but its long-term evolution over several of linear growth times by means of hydrodynamical simulations. This is important because the dynamical time-scales of the processes where we can observe the shear layers operate on much longer time-scales than the linear growth time of the KHI;
(iii) derive an empirical relation for the viscous KHI growth time as a function of Reynolds number and density contrast;
(iv) show that also a strongly temperature-dependent Spitzer-like viscosity can suppress the KHI.

The paper is organized as follows. In Section 2 we summarize relevant previous results on the KHI and analytically derive a critical Reynolds number below which the KHI is suppressed. Section 3 describes the simulation set-up and method. Section 4 reports the results of the simulations, and Section 5 discusses implications of our results. We summarize our findings in Section 6.

2 KHI IN VISCOUS FLUIDS – ANALYTIC CONSIDERATIONS

The KHI arises due to a shear flow parallel to the interface between two fluids. In the most simple case, two incompressible inviscid fluids of densities $\rho_{\rm hot}$ and $\rho_{\rm cold}$ but equal pressures are separated by a planar interface. While the temperature is still irrelevant at this point we choose this notation for consistency with later discussions in the paper. We consider the 2D case and place the interface at $y = 0$. Without loss of generality, the hot and cold fluid move with velocities $U/2$ and $-U/2$ parallel to the interface, i.e. they are subject to a mutual shear flow. At the interface, both the velocity and density change discontinuously (the densities can also be identical). If a perturbation of length scale λ is introduced at the interface, the perturbation grows exponentially with a growth time of

$$\tau_{\rm KHinvisc} = \frac{\sqrt{\Delta}}{2\pi}\frac{\lambda}{U} = 3.9\,{\rm Myr}\,\sqrt{\Delta}\frac{\lambda}{10\,{\rm kpc}}\left(\frac{U}{400\,{\rm km\,s^{-1}}}\right)^{-1} \quad (2)$$

$$\text{with } \Delta = \frac{(\rho_{\rm cold}+\rho_{\rm hot})^2}{\rho_{\rm cold}\rho_{\rm hot}} = D_\rho(1+1/D_\rho)^2 \quad (3)$$

$$\text{and } D_\rho = \frac{\rho_{\rm cold}}{\rho_{\rm hot}}.$$

This standard scenario and many variations e.g. the presence of compressibility (see Appendix A), gravity, surface tension and magnetic fields have been discussed in textbooks (e.g. Lamb 1932; Chandrasekhar 1961; Drazin & Reid 2004).

The case of viscous KHI is missing from the extensive discussions in the textbooks because the background flow is not steady. The standard approach of linear perturbation analysis assumes a background state for the spatial distribution of fluid density ρ, pressure p and velocity U. In the case of the KHI this is the shear flow described in the beginning of this section. Then small

perturbations $u \ll U$, and equivalents for other quantities, are added to the background flow. Quantities like $U + u$ are inserted into the hydrodynamical equations, and these are linearized. Following this approach for the KHI leads to a system of equations for the perturbed quantities like in equations (6)–(10) in Junk et al. (2010) or equations (A1)–(A6) in Kaiser et al. (2005). However, both of these works made the additional assumption that the background flow is steady, i.e. $\partial U/\partial t = 0$. This is true *only* if the viscosity is small. A non-negligible viscosity, however, smoothes out the shear velocity gradient across the interface, i.e. $\partial U/\partial t \neq 0$ even without any perturbation. If this aspect is taken into account, the term $\delta\rho \frac{\partial U}{\partial t}$ needs to be added to the left-hand side of equation (A1) in Kaiser et al. (2005) and equation (6) in Junk et al. (2010), where $\delta\rho$ is the density perturbation. This term breaks the symmetry of the linearized equations and makes the calculation of a dispersion relation cumbersome.

Nonetheless, we can estimate the behaviour of the KHI at low and high viscosities. Naturally, at low viscosities the KHI approaches the inviscid case described above. A high viscosity must suppress the KHI below certain length scales for the following reason: the effect of viscosity is to smooth out the velocity gradient between both fluid layers by momentum diffusion (see also Section B2). If, however, in the classic KHI set-up the discontinuity in the shear velocity is smoothed over a length scale $\pm d$ above and below the interface, the KHI is inhibited for wavelengths smaller than $\sim 10\,d$ (Chandrasekhar 1961, section 102). Consequently, a given viscosity must suppress the KHI below a certain length scale. We can estimate this limit quantitatively as follows.

In the inviscid case with a discontinuous shear velocity, a perturbation of wavelength λ grows on the time-scale of $\tau_{\rm KHinvisc}$ (equation 2). During one $\tau_{\rm KHinvisc}$, a given viscosity ν widens the jump in shear velocity to the diffusion length $l_D(t = \tau_{\rm KHinvisc}) = \pm 2\sqrt{\nu \tau_{\rm KHinvisc}}$ around the interface. Consequently, all perturbations with wavelengths $< 10 l_D(\tau_{\rm KHinvisc})$ cannot become KH unstable. Thus, the growth of the perturbation of wavelength λ will be suppressed if

$$\lambda < 10 l_D(\tau_{\rm KHinvisc}) = 20\sqrt{\nu \tau_{\rm KHinvisc}} \quad \text{or} \tag{4}$$

$$\nu > \nu_{\rm crit} = \frac{\pi}{200}\frac{\lambda U}{\sqrt{\Delta}} \quad \text{or} \tag{5}$$

$$\mathrm{Re} = \frac{\lambda U}{\nu} < \mathrm{Re}_{\rm crit} \approx 64\sqrt{\Delta}. \tag{6}$$

Here and in the following, we define the Reynolds number for the KHI as

$$\mathrm{Re} = \frac{\lambda U}{\nu}, \tag{7}$$

where U is the shear velocity, i.e. the difference in velocity between both layers, λ the perturbation length and ν the kinematic viscosity. Note that in other work the length scale used in the Reynolds number may refer to an initial width of the interface instead to the perturbation length. Equation (6) shows that the KHI should be suppressed not only for Reynolds numbers around 1, but already for Reynolds numbers around 130, with a moderate dependence on density contrast.

Viscosity continuously broadens the jump in shear flow, and the choice of comparing the perturbation length scale λ to the diffusion length l_D at $t = \tau_{\rm KHinvisc}$ is somewhat arbitrary. However, two different considerations arrive at similar estimates. The viscous broadening of the interface should dominate and suppress the KHI if the viscous dissipation time-scale $\tau_\nu = L^2/\nu$ is shorter than the KHI growth time. For the former, L is the length scale of velocity gradients that need to be dissipated. As noted above, the KHI at length scale λ is suppressed if the shear flow jump is smoothed over $\sim\lambda/10$; hence we use $L = \lambda/10$. This leads to

$$\frac{\sqrt{\Delta}}{2\pi}\frac{\lambda}{U} = \tau_{\rm KHinvisc} > \tau_\nu = \frac{L^2}{\nu} = \frac{(\lambda/10)^2}{\nu} \quad \text{or} \tag{8}$$

$$\mathrm{Re} < \mathrm{Re}_{\rm crit} \approx 16\sqrt{\Delta}, \tag{9}$$

as the condition to suppress the KHI.

A third estimate comes from demanding that the height of the unsuppressed KH rolls would lag behind the viscous broadening of the shear flow jump up to the time the final height is reached. The inviscid KHI saturates after $\sim 4\tau_{\rm KHinvisc}$, and the rolls reach a height of typically $\lesssim \lambda/2$, with small perturbations only $\lambda/4$. Consequently, the condition for a suppressed KHI is

$$\lambda/2 < l_D(4\tau_{\rm KHinvisc}) = 2\sqrt{\nu 4\tau_{\rm KHinvisc}} \quad \text{or} \tag{10}$$

$$\mathrm{Re} < \mathrm{Re}_{\rm crit} \approx 10\sqrt{\Delta}. \tag{11}$$

This third estimate is rather conservative. For example, assuming $\lambda/4$ as the height of the KH rolls leads to a four times higher $\mathrm{Re}_{\rm crit}$, which is close to our first estimate. Thus, our estimates agree within order of magnitude that viscosity should certainly suppress the KHI for Re < several 10s. Our simulations confirm this general result. However, they show that the dependence on density contrast derived here is wrong because none of our estimates takes into account that the viscous broadening of the shear flow jump proceeds asymmetrically between two layers with different densities.

Earlier work on viscous shear flows reaches similar conclusions (e.g. Esch 1957; Amsden & Harlow 1964; Gerwin 1968). Villermaux (1998) investigates the stability of a viscous shear flow layer where the jump in velocity is already smoothed over a certain width $2d$. A given smoothing of the velocity jump does not only prevent the KHI at small wavelengths but also reduces the maximum growth rate. The author stresses that, especially for small initial widths, the viscous spreading can occur faster than the KHI, and even if the KHI should still grow formally, it would not show up because it is not the fastest process. By comparing the viscous spreading rate to the KHI growth rate given the evolving viscously spreading interface, Villermaux (1998) estimates the critical wavelength $\lambda_{\rm crit}$ below which the KHI is suppressed as a function of viscosity. In the limit of small initial widths, his equation (13) can be rewritten as

$$\frac{\lambda_{\rm crit} U}{\nu} = \frac{2\pi}{b} 10a, \tag{12}$$

expressing his result in terms of our Reynolds number. The parameters a and b are factors of order unity, depending on the exact shape of the smoothed velocity jump. This result agrees well with our simpler order-of-magnitude estimates.

3 NUMERICAL SIMULATIONS – METHOD

3.1 Model set-up

We set up a 2D simulation box with a cool gas below $y = 0$ and a hot gas above. The shear flow is set as constant velocities $U/2$ and $-U/2$ in x-direction, i.e. parallel to the interface, in the hot and cold fluid, respectively. Our standard choice is a shear velocity U

corresponding to Mach 0.5 in the hot layer. We introduce a sinusoidal perturbation in the velocity component v_y, i.e. perpendicular to the interface, of amplitude v_0 and wavelength λ. The perturbation is restricted to the layer around the interface and decreases away from it as in Junk et al. (2010):

$$v_y = v_0 \sin\left(\frac{2\pi x}{\lambda}\right) \exp\left(-\left[\frac{y}{\sigma_y}\right]^2\right). \quad (13)$$

The scale parameter for the width of the perturbation layer is $\sigma_y = 0.3\lambda$, the perturbation amplitude is $v_0 = 0.1U$. We verified that the suppression of KHI by viscosity does not arise due to an insufficient perturbation (see Appendix D and Fig. D1). Our simulation box has the size of $(-\lambda, \lambda)$ and $(-2\lambda, 2\lambda)$ x- and y-direction, respectively. We verified that the simulation box is sufficiently large in y-direction to ensure an unimpeded growth of the KHI by re-simulating some cases with particularly tall KHI rolls with a simulation box twice as high. The simulation box is periodic in x-direction and has open boundaries in y-direction. We chose this set-up over an all-periodic set-up because it is a better representation of real situations where the shear flow arises, e.g. at CFs. For subsonic shear velocities relative to the hot layer the open boundaries lead to a mass and energy loss from the simulation volume of less than 1 or 2 per cent over the course of the simulations, which is irrelevant. We arrive at very similar results when using reflecting boundaries in y-direction, but sound and shock waves originating at the interface are reflected at the boundaries and make the evolution noisier. For supersonic shear flows mass losses are still below 4 per cent, but shocks leaving the simulation box lead to a loss of total energy of up to 10 per cent at high viscosities. Shock waves carrying away energy from the shear layer is, however, a realistic effect.

The set-up described so far employs discontinuities in density and shear velocity at the interface. In low-viscosity simulations this set-up is prone to secondary, unintended KHI modes at length scales $<\lambda$ that are seeded by the numerical discretization. However, the viscosity included in our simulations prevents these secondary modes for most cases, and we use the straightforward set-up with the discontinuous interface. This also ensures that the KHI has the best-possible chance to grow and is not slowed down by an initially smoothed interface. Only at high Re do the secondary modes appear. There we follow the suggestion of McNally, Lyra & Passy (2012) and slightly smooth the density and shear velocity jump according to

$$X(y) = \begin{cases} X_{\rm cold} - X_m \exp(y/w) & \text{if } y \le 0, \\ X_{\rm hot} + X_m \exp(-y/w) & \text{if } y > 0, \end{cases} \quad (14)$$

$$\text{with } X_m = (X_{\rm cold} - X_{\rm hot})/2 \quad (15)$$

and $X \in \{\rho, v_x\}$.

The smoothing scale length is 1–2 per cent of λ, which does not affect the growth of the intended mode. Secondly, we apply this smoothing in simulations with high density contrasts and high viscosity, where viscous dissipation would lead to excessive heating at a discontinuous interface.

3.2 Code

We use the FLASH code (version 3.3; Dubey et al. 2009). FLASH is a modular block-structured adaptive mesh refinement code, parallelized using the Message Passing Interface (MPI) library. It solves the Riemann problem on a Cartesian grid using the Piecewise Parabolic Method (PPM). We solve the viscous hydrodynamic equations (e.g. Landau & Lifschitz 1991; Batchelor 2000):

$$\frac{\partial \rho}{\partial t} + \nabla \cdot (\rho \boldsymbol{v}) = 0 \text{ (continuity eqn.)}, \quad (16)$$

$$\frac{\partial \rho \boldsymbol{v}}{\partial t} + \nabla \cdot (\rho \boldsymbol{v}\boldsymbol{v}) + \nabla \cdot \boldsymbol{\Pi} = 0 \text{ (momentum eqn.)}, \quad (17)$$

$$\frac{\partial \rho E}{\partial t} + \nabla \cdot (\rho E \boldsymbol{v}) + \nabla \cdot (\boldsymbol{\Pi} \cdot \boldsymbol{v}) = 0 \text{ (energy eqn.)}, \quad (18)$$

where ρ is the mass density, E the specific total energy and $\boldsymbol{v}$ the gas velocity. We assume an ideal equation of state with $\gamma = 5/3$. The full pressure tensor $\boldsymbol{\Pi}$ includes the viscous stresses:

$$\Pi_{ik} = \delta_{ik} P - \pi_{ik} \text{ with}$$

$$\pi_{ik} = \mu \left(\frac{\partial v_i}{\partial x_k} + \frac{\partial v_k}{\partial x_i} - 2/3\, \delta_{ik} \nabla \cdot \boldsymbol{v}\right). \quad (19)$$

Here, μ is the dynamic shear viscosity, and we neglect the second viscosity. In the inviscid case with $\mu = 0$ we recover the Euler equations, where only the isotropic pressure P appears in the momentum and energy equations. Viscous fluxes for momenta and energy are computed explicitly. We verified the accuracy of the viscosity module on two set-ups with analytic solutions: the viscous flow between two stationary plates, and the viscous spreading of a shear flow discontinuity (see Appendix B).

3.3 Types of viscosity

The nature of the viscosity in the ICM is unknown, it may be constant or strongly temperature dependent. Thus, we investigate the impact of a constant kinematic viscosity ν and a Spitzer-like kinematic viscosity $\nu_{\rm Sp} = A_\mu T^{5/2}/n$. The viscosity amplitude A_μ is varied to achieve Reynolds numbers between $\sim$10 and 10^4, thus sampling the range of possible Re in the ICM (see equation 1 and Section 5.1). Because of its temperature and density dependence, a Spitzer-like viscosity leads to strong dependence of the ratio of Reynolds numbers in the hot and the cold layer on density contrast $D_\rho = \frac{\rho_{\rm cold}}{\rho_{\rm hot}}$:

$$D_{\rm Re} = \frac{{\rm Re}_{\rm cold}}{{\rm Re}_{\rm hot}} = D_\rho^{7/2}. \quad (20)$$

In the case of a constant kinematic viscosity, the Reynolds number is the same in both layers.

We discuss limits on plausible Reynolds numbers in the ICM due to the related length of the mean free path and saturation of momentum transport in Section 5.1.

3.4 Resolution

We use a uniform grid and a standard resolution of 128 cells per perturbation length. In Appendix E we demonstrate convergence of our results. Furthermore, in Appendix E we show that the FLASH code captures the presence and size of KH rolls down to a resolution 16 grid cells per perturbation length. The internal structure of the KH rolls, e.g. regarding mixing and velocity structure, requires a higher resolution that ensures that the width, or thickness, of the KHI mixing layer is resolved beyond the numerical diffusion length of 2–3 grid cells.

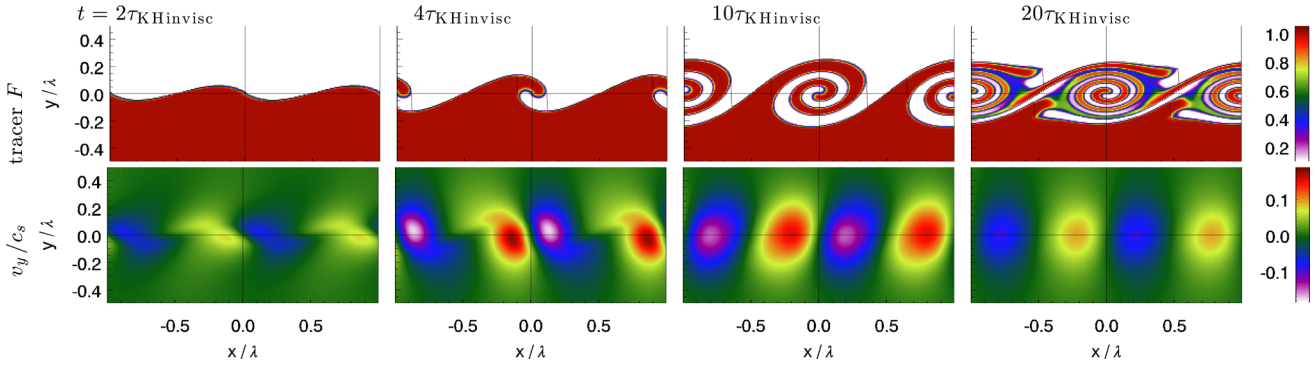

Figure 1. The top row shows snapshots of the tracer F for a fiducial Kelvin–Helmholtz test. Initially, the tracer was $F = 1$ for $y < 0$ and $F = 0$ for $y \geq 0$. Time-steps from left to right are labelled above each column. This simulation used a spatially constant kinematic viscosity ν, a density ratio $D_\rho = 1$ between both layers, a shear flow of Mach 0.5 and a Reynolds number of Re = 1000 (see equation 7). Snapshots for other Re are shown in Fig. 2. The thin black lines mark the 'edges' of the upper and lower fluid, used to measure the height of the KH rolls, see Section C1. The growth of the KHI rolls is shown in the top panel of Fig. 3. The bottom row colour codes the vertical velocity v_y in units of the sound speed c_s at corresponding times, highlighting the vortices due to the KH rolls. The temporal evolution of the maximum v_y is shown in the bottom panel of Fig. 3. Note that the simulation box extends in y-direction from -2λ to 2λ, i.e. beyond the size of the snapshots.

4 SIMULATION RESULTS

4.1 Fiducial KHI – density ratio 1, constant kinematic viscosity, Reynolds number 1000

Fig. 1 displays the typical evolution of the KHI for the most simple case with equal densities in both layers. A low viscosity is applied to achieve Re = 1000. At this Reynolds number, the KHI at the intended perturbation length is slightly slowed down by viscosity but unintended secondary modes are absent, making this case instructive. Because of the uniform density throughout the simulation box we use a tracer to visualize the two fluid layers. Initially, the tracer was set to $F = 1$ for $y < 0$ and $F = 0$ for $y \geq 0$. The evolution of the tracer fluid is displayed in the top row of Fig. 1. The bottom row displays the distribution of v_y, i.e. the velocity component perpendicular to the initial interface.

The instability evolves in two phases, a growth phase followed by a saturation phase. During the first ∼3–4$\tau_{\rm KHinvisc}$ the initial perturbation leads to a wave-like distortion of the interface. Simultaneously, $v_{\rm ymax}$, the maximum of the vertical velocity, increases to up to four times the initial perturbation amplitude. At the end of this growth phase the interface starts to roll up, leading to the classic KH roll or cat-eye pattern over the next few $\tau_{\rm KHinvisc}$. In the following saturation phase, these rolls continue to spin over many $\tau_{\rm KHinvisc}$. The low viscosity slowly dissipates the vortices, decreasing $v_{\rm ymax}$. The height of the rolls, or the thickness of the mixing layer, increases until about $8\tau_{\rm KHinvisc}$ and then saturates as well. Given that we introduced only a single perturbation mode with a length scale of half the box width, the simulation box contains only two identical KHI rolls. In a more realistic perturbation spectrum, small perturbations start growing first, and with time larger and larger perturbations dominate the appearance.

4.2 Constant kinematic viscosity

Next we investigate the effect of varying the viscosity. In this section we apply a spatially constant kinematic viscosity, which leads to equal Reynolds numbers in both layers regardless of density contrast.

4.2.1 Density ratio 1

We start with the equal density case. Fig. 2 displays the evolution of the instability for Reynolds numbers between 100 and 10^4. Fig. 3 shows the evolution of the width of the KHI-induced mixing layer (top), and of $v_{\rm ymax}$ (bottom). Section C explains how both quantities are measured, and how the viscous KHI growth time is measured from $v_{\rm ymax}(t)$.

As indicated above, the evolution of the viscous KHI is governed by the competition of the actual instability and viscosity. The former increases the height of the KH rolls and leads to an exponential growth of velocities in y-direction. Indeed, for Re = 10^4, the exponential growth time of $v_{\rm ymax}$ recovers the analytic estimate for the inviscid KHI growth time $\tau_{\rm KHinvisc}$. Viscosity, on the other hand, dissipates velocity gradients. A low viscosity cannot slow down the widening of the mixing interface, but the rolling up of the KH rolls. Already at Re = 1000 the rolls curl up slower than at Re = 10^4 (Fig. 2). At Re = 300 only rudimentary rolls are formed, and at lower Re the interface does not roll up at all. For Re $\lesssim$ 300 also the width of the mixing layer, or height of the KH rolls, is reduced. This visual impression from Fig. 2 is confirmed in the upper panel of Fig. 3. The dissipation of velocity shear becomes clear in the bottom panel of Fig. 3. Instead of a saturation of $v_{\rm ymax}$ at late times like in the Re = 10^4 case, higher viscosities lead to an approximately exponential decrease. The decay time is shorter for lower Reynolds numbers, which translates into the reduced curling-up of the KH rolls. Furthermore, the peak value of $v_{\rm ymax}$ is reduced with increasing viscosity, and the initial exponential growth of $v_{\rm ymax}$ is slowed down with decreasing Re. Below Re = 200 there is no initial growth anymore, the instability is suppressed. This agrees with the drastic reduction of the mixing layer width with decreasing Re.

We summarize the influence of viscosity in Fig. 4 by plotting the measured viscous KH growth times as a function of Reynolds number. The black crosses are for the equal density case. The viscous growth time increases strongly from Re = 1000 down to Re = 300. Below Re ∼ 200 growth times are negative, i.e. the instability is suppressed. Thus, the numerically derived critical Reynolds number is even about 50 per cent higher than the analytic estimate in equation (6).

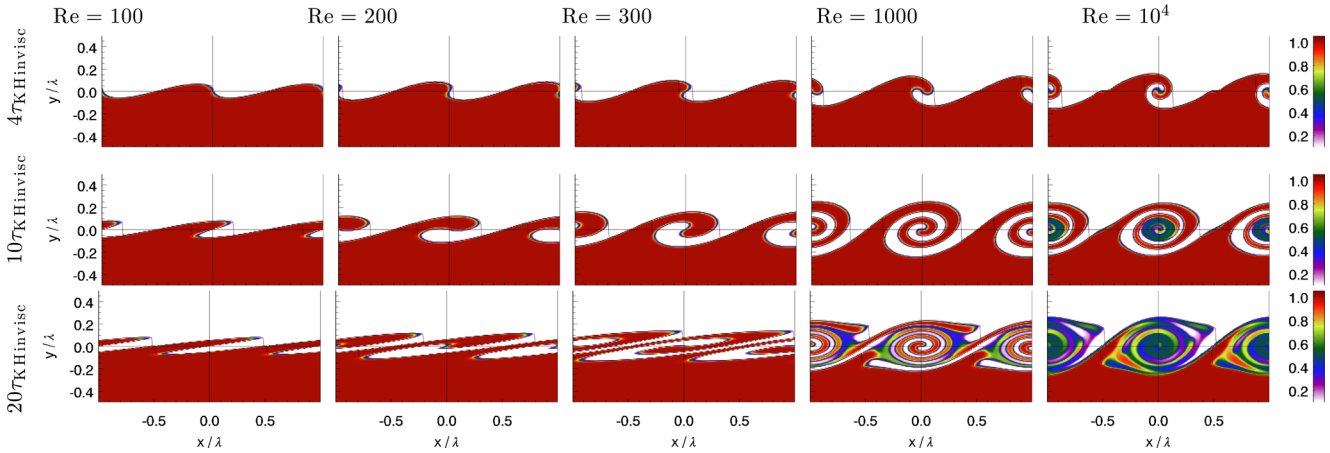

Figure 2. Snapshots showing the tracer F for various Reynolds numbers (labels at top of each column) and three time-steps (labels on the left). These simulations used a constant kinematic viscosity ν, a density contrast $D_\rho = 1$ and a shear flow of Mach 0.5. The KHI is significantly slowed down below $\mathrm{Re} \leq 300$. For $\mathrm{Re} \leq 200$, the deformation of the interface is solely due to the initial perturbation, i.e. the KHI itself is suppressed. Fig. 3 compares the height of the KH rolls and the evolution of the maximal vertical velocity. For $\mathrm{Re} = 10^4$ we smoothed the initial interface over 1 per cent of the perturbation length scale to suppress secondary instabilities (see equation 14).

The dependence of the numerically derived growth times on Reynolds number can be approximated by the empirical relation:

$$\tau_{\mathrm{KHvisc}} = \tau_{\mathrm{KHinvisc}} \left(1 + \frac{\mathrm{Re}_0}{\mathrm{Re} - \mathrm{Re}_{\mathrm{crit}}}\right) \quad \text{for } \mathrm{Re} > \mathrm{Re}_{\mathrm{crit}}, \tag{21}$$

where $\mathrm{Re}_{\mathrm{crit}}$ is the critical Reynolds number below which the KHI is suppressed, and Re_0 scales the decrease of τ_{KHvisc} with Re. For the case of equal densities the numeric values of $\mathrm{Re}_{\mathrm{crit}} = 220$ and $\mathrm{Re}_0 = 660$ fit the simulation results as shown by the black line in Fig. 4. The dependence of $\mathrm{Re}_{\mathrm{crit}}$ and Re_0 on density contrast is given in equations (22) and (23) below.

4.2.2 *Density contrasts up to 10*

Figs 5 and 6 display tracer slices for the viscous KHI for density ratios $D_\rho = 2$ and 10 between the two layers, respectively. The unequal densities between both layers result in an asymmetric evolution of the KHI. The fingers or filaments of cool gas are thinner than the hot ones because the denser gas has more inertia and is thus more difficult to displace. The KHI rolls extend further into the hot layer than into the cold layer, and the growth times of $v_{y\mathrm{max}}$ and $v_{y\mathrm{min}}$ differ slightly. We took this into account in Fig. 7 by measuring the height of the KH rolls above and below the initial interface, and by distinguishing between $v_{y\mathrm{max}}$ and $v_{y\mathrm{min}}$ instead of using only $v_{y\mathrm{max}}$. At the higher density contrast of 10 and high Re, the late evolution of the KHI takes on more complex dynamics.

The impact of viscosity is very similar as in the $D_\rho = 1$ case. The dissipation of velocity shears again leads to reduced rolling up of the interface, slower growth times, decreasing heights of the KHI rolls and finally suppression of the KHI at low Reynolds numbers. For $D_\rho = 2$, the limiting Re is similar to the $D_\rho = 1$ case. For $D_\rho = 10$ the growth rates derived from $v_{y\mathrm{max}}(t)$ and $v_{y\mathrm{min}}(t)$ imply that the KHI still grows initially for $\mathrm{Re} = 100$. However, the height of the distortions of the interface remains well behind the $\mathrm{Re} \geq 300$ case, and the interface does not roll up. Therefore we consider the KHI suppressed in this case as well. Nonetheless, at the higher density contrast, viscosity seems to be less able to slow down the KHI. For example, at $\mathrm{Re} = 300$, the derived growth time is only slowed down by a factor of 3 compared to the inviscid case, whereas at lower density contrast it was slowed down by a factor of almost 10. A closer look at the dynamics reveals that viscosity does not only need to work against the KHI, but also against the increased amount of momentum in the denser layer. We revisit this point in Section 4.4.

We again summarize the influence of viscosity in Fig. 4 by plotting the measured viscous KH growth times as a function of Reynolds number. Symbols of different colours code different D_ρ. Again, we can approximate $\tau_{\mathrm{KHvisc}}(\mathrm{Re})$ by equation (21) but parameters $\mathrm{Re}_{\mathrm{crit}}$ and Re_0 depending on D_ρ. The variation of $\mathrm{Re}_{\mathrm{crit}}$ and Re_0 with density contrast can be approximated by

$$\mathrm{Re}_{\mathrm{crit}} = 880/\Delta, \tag{22}$$

$$\mathrm{Re}_0 = 1320/\sqrt{\Delta}, \tag{23}$$

where Δ depends on the density contrast D_ρ as in equation (4). Thus, equation (21) combined with equations (22) and (23) provides an empirical relation for the viscous KHI growth time as a function of Re up to density contrasts of 10. This empirical relation is shown by lines of matching colour in Fig. 4. We note that due to being based solely on the evolution of the v_y extrema, this empirical relation slightly underestimates the ability of the viscosity to suppress the KHI at high density contrasts. For $D_\rho = 10$ it states $\mathrm{Re}_{\mathrm{crit}} = 73$, but we discussed above that the KHI is already suppressed for $\mathrm{Re} = 100$. If viewed in detail, the suppression of the KHI by viscosity is a gradual process, and the difference in $\mathrm{Re}_{\mathrm{crit}}$ arises due to a different definition of when suppression of the KHI is reached. Thus, the empirical relation is useful within a factor of 1.5.

Our simulations find that $\mathrm{Re}_{\mathrm{crit}}$ slightly decreases with density contrast, which is opposite of what was expected from all analytical estimates in Section 2. The reason is that none of those estimates takes into account that the diffusion of momentum into the denser, cold layer will be slower due to the higher momentum in the dense layer. The slower diffusion of momentum into the cold layer leads to a slower widening of the shear flow discontinuity into the cold layer, and hence only smaller instabilities can be

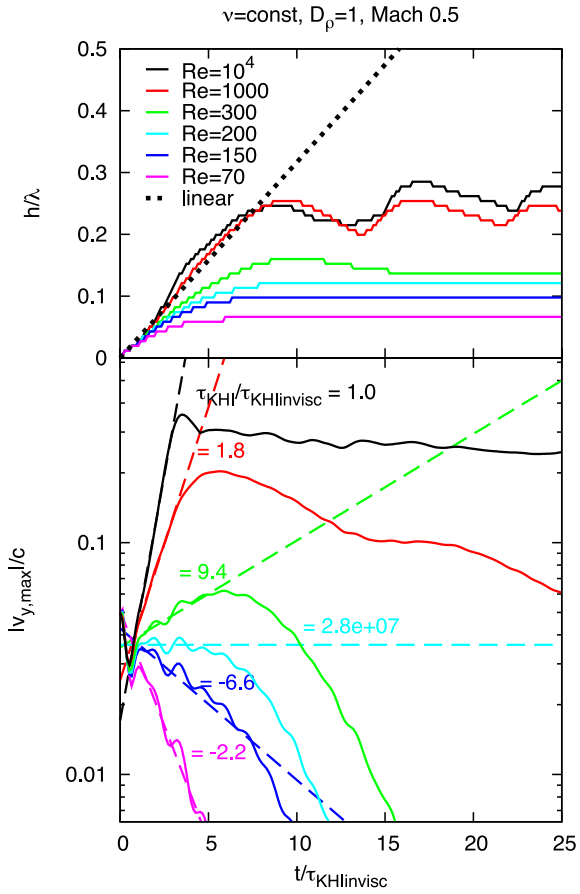

Figure 3. Temporal evolution of the height of the KH rolls (top) and of the maximum velocity in y-direction, $|v_y|_{\max}$ (bottom). Different line colours code different Reynolds numbers, see legend. Figs 1 and 2 display corresponding snapshots. All runs are for a constant kinematic viscosity, $D_\rho = 1$, and shear flow = Mach 0.5. In the top panel, the expected linear increase of the interface distortion as it would occur purely due to the initial perturbation is shown as the black dotted line labelled 'linear'. The smaller height of the KH rolls for Re ≤ 300 is due to viscosity. The maximum v_y shows an initial exponential growth for Re $\gtrsim 200$. After $\sim 5\tau_{\rm KHinvisc}$, $v_{\rm ymax}$ decreases approximately exponentially due to viscous dissipation, i.e. faster for lower Reynolds numbers. We fit the initial increase with exponential functions that are shown as thin dashed lines of matching colour. The resulting growth times are stated in the plot in units of $\tau_{\rm KHinvisc}$ in corresponding colours. The initial exponential growth time is the viscous KHI growth time (see also Section 4.2.1, Fig. 4 and Appendix C). Note that we ignore the initial fluctuations of $v_{\rm ymax}$ during the first $\tau_{\rm KHinvisc}$ because they reflect sound waves from the initialization and not the KHI growth.

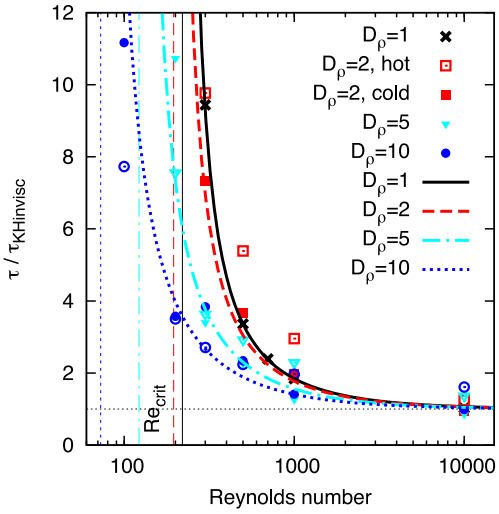

Figure 4. Viscous KHI growth time as a function of Reynolds number and density contrast, for the case of a spatially constant kinematic viscosity. Colours code the density contrast, see legend. The symbols show the growth times derived from the maximum and minimum v_y. For density contrasts >1, open symbols show the growth time derived from the maximum v_y, i.e. velocities towards the hot layer, solid symbols show the minimum v_y, i.e. derived from the fastest velocity towards the cold layer. For equal densities, the KHI evolves symmetrically, and only one symbol is shown. Lines show the empirical relation given equation (21) combined with equations (22) and (23). We mark the critical Reynolds number $\mathrm{Re_{crit}}$, below which the KHI does not grow at all, with vertical lines of matching colour.

suppressed – or, stated differently, a lower Re is required to suppress a given perturbation.

4.3 Spitzer viscosity

The density dependence and strong temperature dependence of the Spitzer-like viscosity introduce a strong difference of Reynolds numbers between the hot and the cold layer. Density contrasts of 2 or 10 result in a ratio of Reynolds numbers of 11 and 3160, respectively. Consequently, the cold layer always will be more turbulent, and we can expect that a higher viscosity is needed to suppress the KHI. The Reynolds number stated in the following refers to the Reynolds number in the hot layer, as this is the crucial one.

Figs 8 and 9 display tracer slices for the Spitzer-viscous KHI. In Fig. 10 we plot the evolution of the height of the KH rolls and of $v_{\rm ymin}$ and $v_{\rm ymax}$ for different Reynolds numbers. Qualitatively, the same trends as before apply. Increasing viscosity slows down the rolling up of the interface, its widening and finally suppresses the instability.

For $D_\rho = 2$ the Spitzer-viscous KHI evolves similarly to the constant ν case except for minor differences. The critical Reynolds number is reduced to 30 compared to 200 in the equal kinematic viscosity case. The KHI is first suppressed on the hot side, i.e. at Re somewhat larger than $\mathrm{Re_{crit}}$ no cool fingers are drawn upwards, but hot fingers can be drawn downwards.

At $D_\rho = 10$, the high density contrast and the highly asymmetric viscosity lead to an untypical and very irregular morphology of the KH rolls also at high Re. At $D_\rho = 2$, the viscosity on the cool side can still add to the suppression of the KHI, whereas at $D_\rho = 10$ the cool side is always turbulent (Re > 1000). This leads to complex flow patterns in the cool layer even if the Reynolds number is low. The initial instability induces vortices in the high-Reynolds number cold gas, which can remain there for a long time. This effect is shown for Re = 10 (in the hot layer) in Fig. 11. Consequently, the maximum and minimum v_y are not a good tracer of an instability anymore, because they mainly trace vortices in the cool gas. Thus, using $v_{\rm ymax}$ and $v_{\rm ymin}$ alone as a diagnostic for the growth of the KHI leads to the impression that the instability is not suppressed at all (right-hand panel of Fig. 10). The evolution of the height of the KH rolls and the snapshots, however, show that the KHI is suppressed for Re $\lesssim 30$. Thus, at high density contrasts, a Spitzer-like viscosity puts the KHI in a hybrid state, where it is able to induce turbulence in the cold layer, but does not mix both fluids.

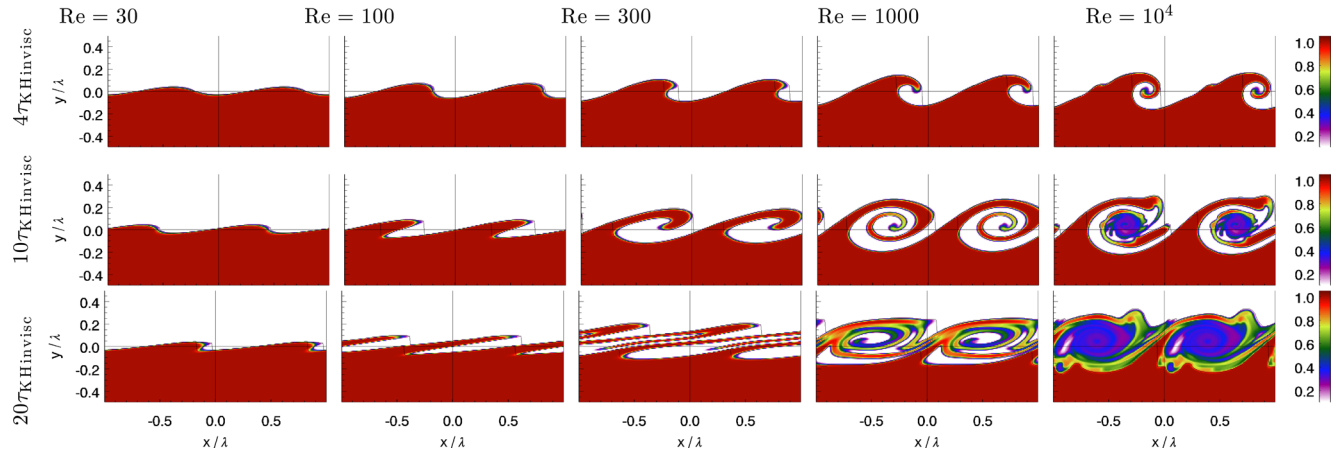

Figure 5. Tracer slices like in Fig. 2, but for constant kinematic viscosity ν, density ratio 2 and shear flow of Mach number 0.5. For Re $= 10^4$ we smoothed the initial interface over 1 per cent of the perturbation length scale to suppress secondary instabilities (see equation 14).

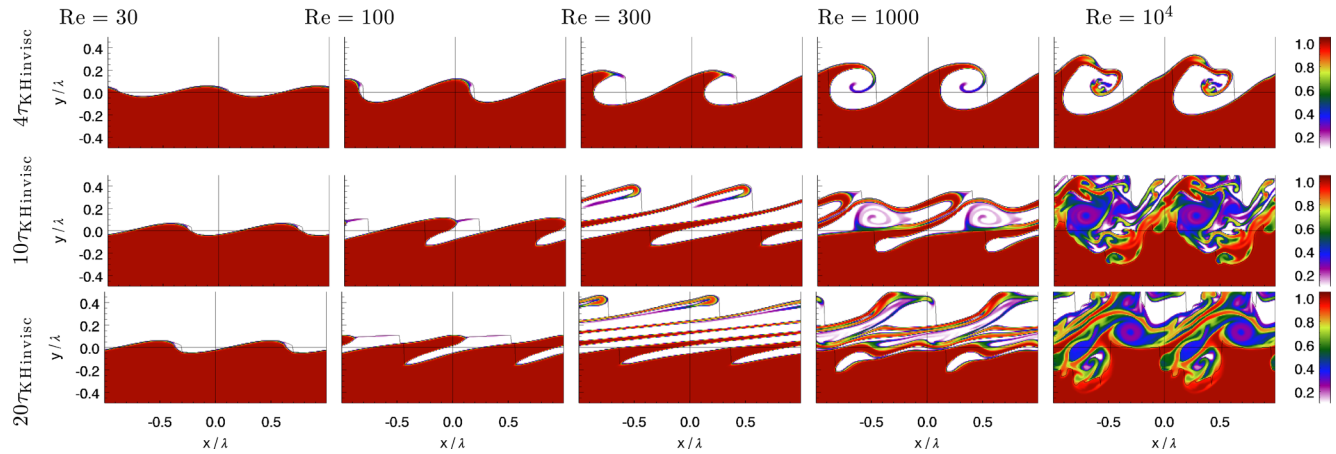

Figure 6. Tracer slices like in Fig. 2, but for constant kinematic viscosity ν, density ratio 10 and shear flow of Mach number 0.5. For Re $= 10^4$ we smoothed the initial interface over 1 per cent of the perturbation length scale to suppress secondary instabilities (see equation 14).

4.4 High density contrast 100

4.4.1 Low viscosity

At even higher density contrasts, the dynamics of the KHI change also at low viscosities. The inertia of the denser layer is enormous, and the flow patterns in the cool dense gas hardly change over many inviscid growth times. At such high density contrasts, the shear velocity is highly supersonic with respect to the cold layer while still subsonic in the hot layer. The cold gas keeps its motion parallel to the interface and the initial perturbation velocity perpendicular to it. Thus, the cold gas causes the interface between both layers to resemble 'growing mountains', over which the wind of hot gas is flowing (Fig. 12). The vertical extent of the mixing layer (height of KH rolls, or distortions) closely follows the linear widening expected from the initial perturbation velocity. Almost all turbulence is induced in the hot gas that flows around the 'mountains' of cold gas. Vortices on the lee side of the 'mountains' form on a time-scale $\sim\lambda/c$, where c is the sound speed of the hot gas. With increasing density contrast the KHI time-scale can exceed the vortex formation time-scale, and the KHI will not dominate the gas flow anymore. Consequently, the maximum or minimum v_y, or any velocity patterns, are not a tracer of the KHI anymore.

Interestingly, after about 3 $\tau_{\rm KHinvisc}$, enough momentum has been transferred from the huge reservoir in the cold layer to the hot gas between the 'cool mountains', such that this hot gas between the cool mountains moves along with the cool gas. Thus results in a *new* shear flow interface at the level of the 'top' of the mountains, and a second generation of KHI evolves. Slightly smoothing the initial interface brings out this effect more clearly (right-hand column of Fig. 12). Without the initial smoothing, numerous secondary instabilities occur. However, the overall dynamics are similar with and without the interface smoothing.

4.4.2 High viscosity

In the case of a constant kinematic viscosity, any instability or turbulence is suppressed for Re ≤ 100 (see Fig. 13). For a Spitzer-like viscosity only the hot gas provides viscosity, and a lower Reynolds number of Re ≤ 10 is needed (Fig. 14). At Re $= 10$, the interface resembles frozen KH rolls, but the instability is not evolving

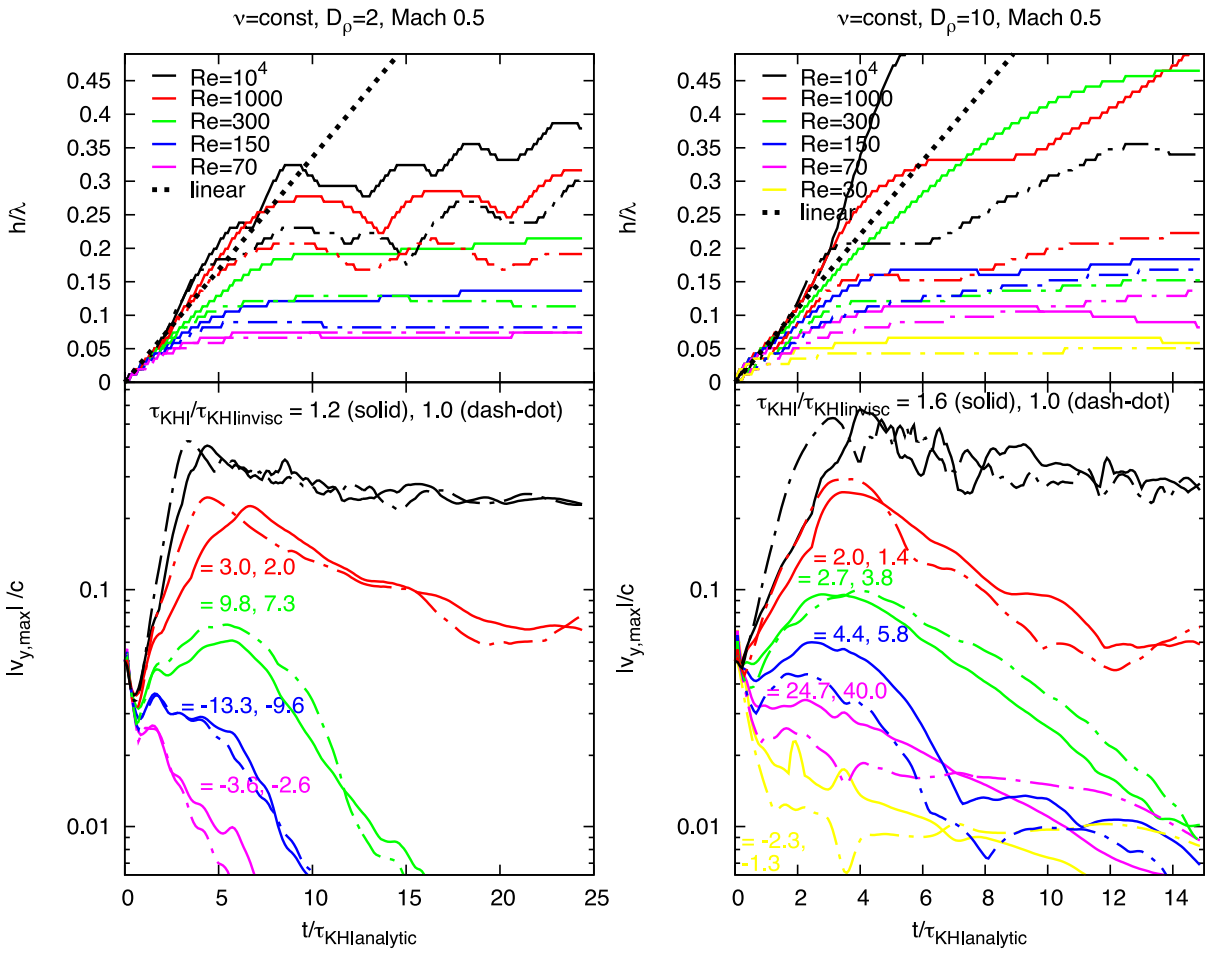

Figure 7. Same as Fig. 3, but for different density contrasts, see title of each column. Because of the unequal densities in the two layers, the KHI evolves asymmetrical, and we plot two lines for each simulation. The solid lines show the evolution towards the hot layer (height of KH rolls above initial interface, maximum of v_y), the dash–dotted lines show the height of KH rolls below initial interface and the minimum of v_y. Exponential growth times for the velocity extrema are given in the bottom panels with the matching font colour. The first number refers to the solid line, the second to the dash–dotted. Qualitatively, the behaviour is very similar to the constant density case, but for a density contrast of 10 a somewhat higher viscosity is needed to fully suppress the KHI.

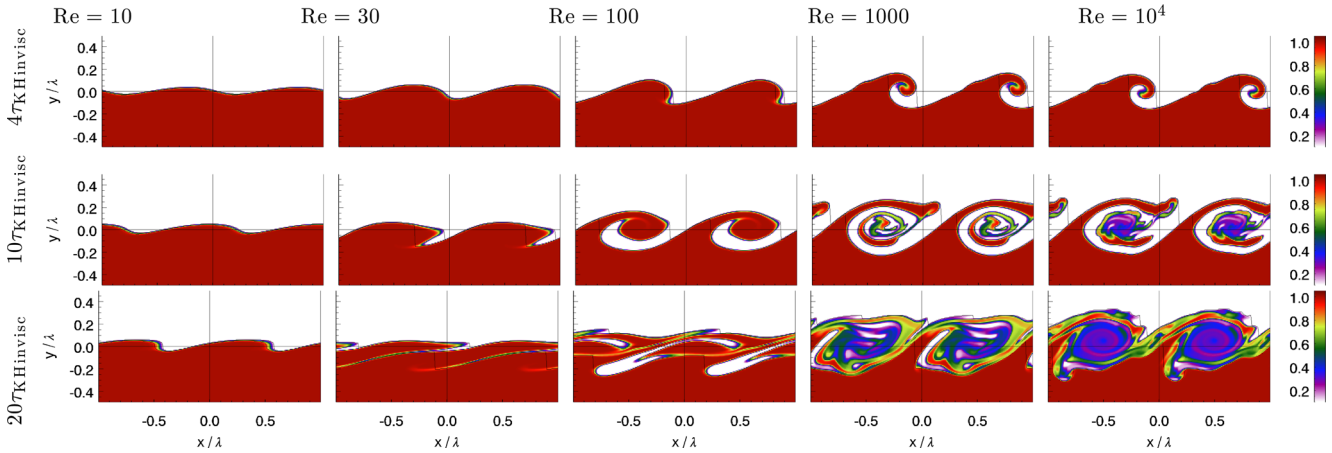

Figure 8. Tracer slices for simulations with Spitzer viscosity, density ratio 2 and shear flow of Mach number 0.5. Columns are for different Re (see top of each column), where the Reynolds number is given for the hot (upper) layer. Re is 11 times higher in the cool (bottom) layer. For Re = 1000 and Re = 10^4 we smoothed the initial interface over 1 and 2 per cent of the perturbation length scale, respectively, to suppress secondary instabilities (see equation 14).

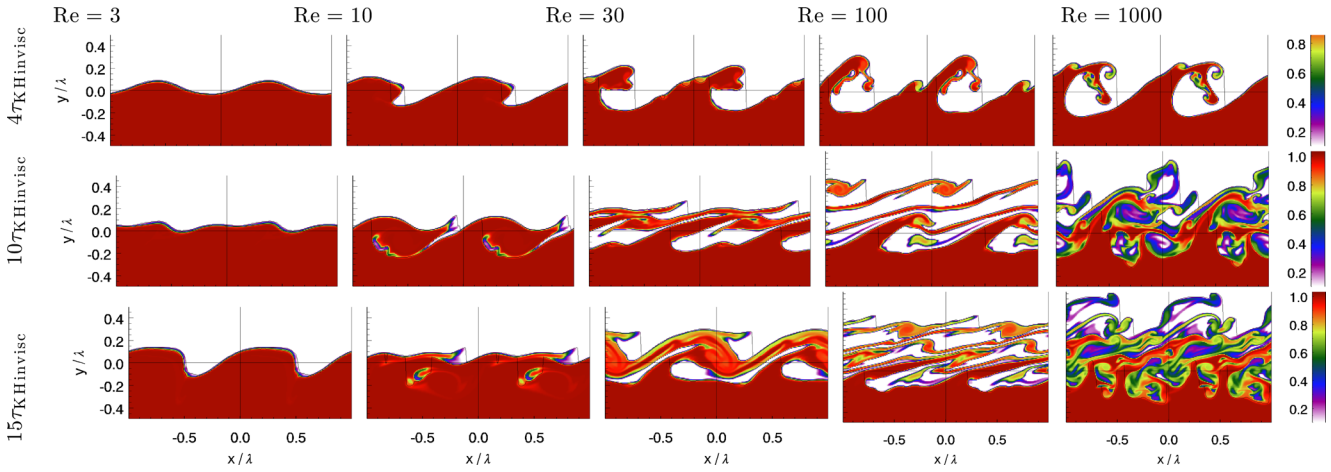

Figure 9. Tracer slices for simulations with Spitzer viscosity, density ratio 10 and shear flow of Mach number 0.5. Columns are for different Re (see top of each column), where the Reynolds number is given for the hot (upper) layer. Re is formally 3000 times higher in the cool (bottom) layer. Fig. 11 shows a zoom-in on the flow patterns for the Re = 10 case. For Re ≥ 30 we smoothed the initial interface over 1 per cent of the perturbation length and for Re = 1000 over 2 per cent of the perturbation length to suppress secondary instabilities (see equation 14).

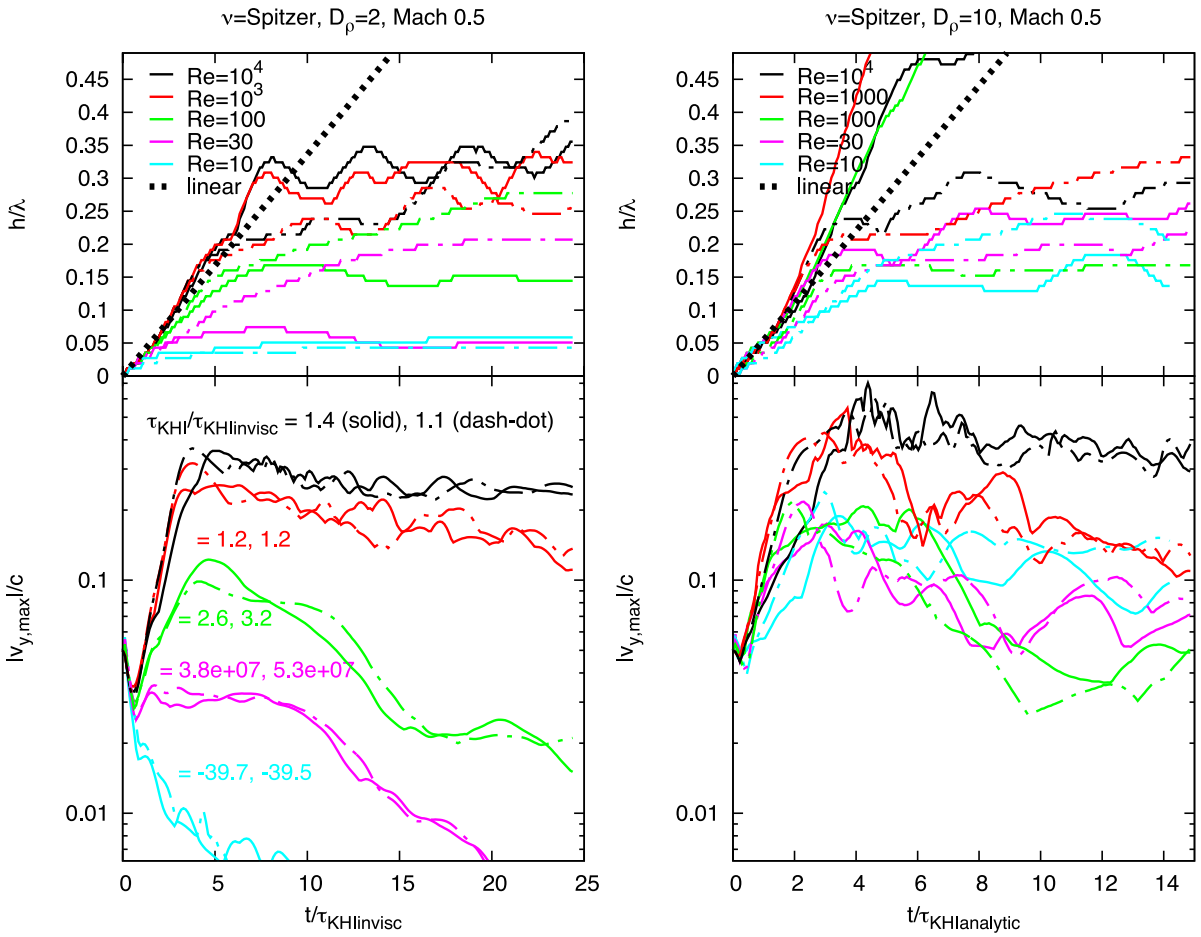

Figure 10. Temporal evolution of the thickness of the KHI mixing layer (top) and of the v_y velocity extrema. All runs are for a Spitzer viscosity and shear flow = Mach 0.5. The two columns are for density contrasts 2 and 10, see label at top. Different line colours code different Reynolds numbers in the hot layer, see legend. Exponential growth times for the velocity extrema are given in the bottom panels with the matching font colour. See Fig. 7 and Section 4.3 for details.

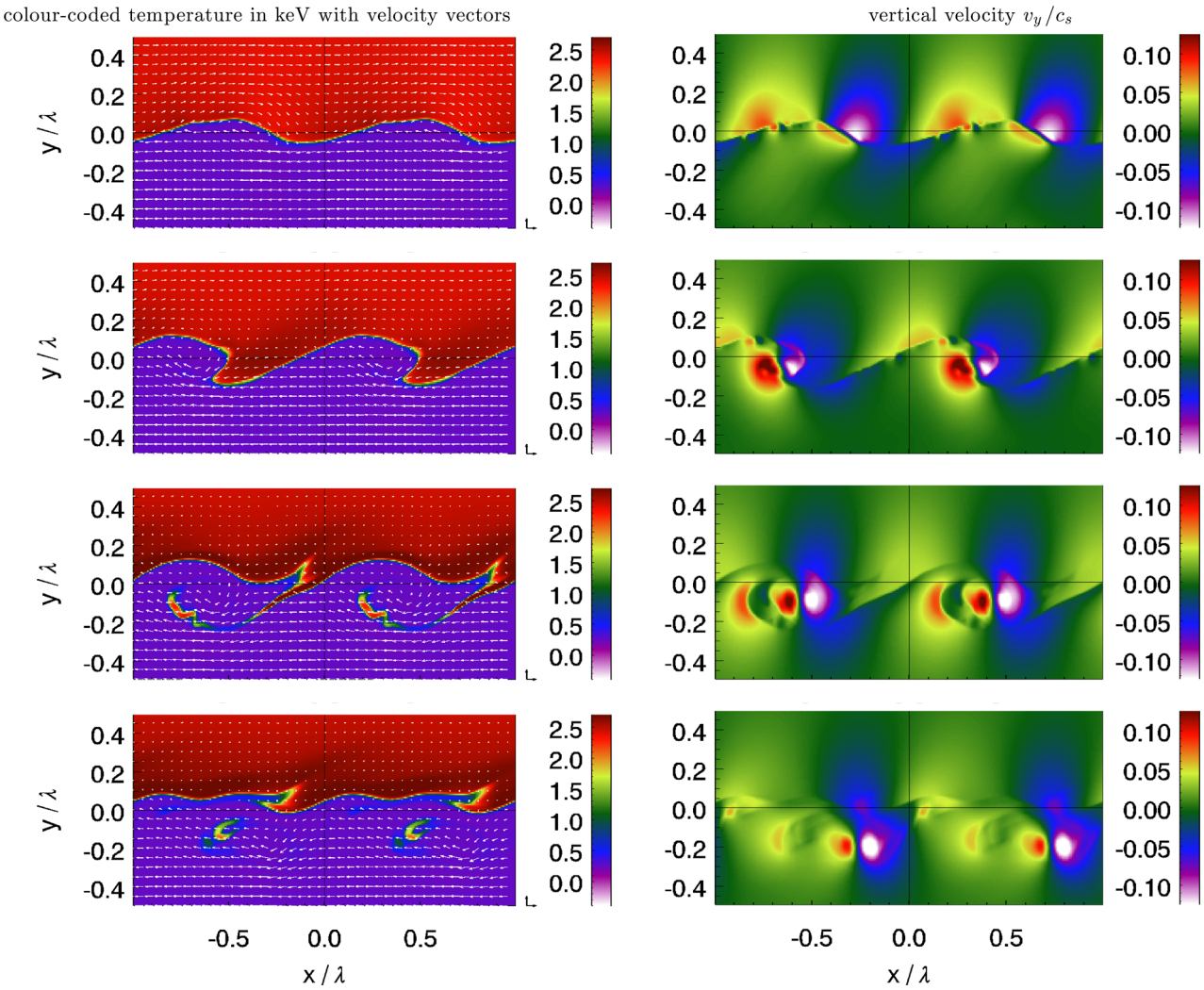

Figure 11. Details of the flow patterns for Spitzer viscosity, density contrast 10, shear flow Mach 0.5 and Reynolds numbers 10 and 3160 in hot and cold layer, respectively. The left-hand column shows the colour-coded temperature in keV with velocity vectors overplotted. The right-hand column colour codes v_y/c_s. The snapshots are at time-steps 2, 4, 10, 15 τ_{KHinvisc} from top to bottom. Note that all turbulence occurs in the cold gas.

anymore. Instead, the hot gas has reversed its direction of motion near the original interface already.

4.5 Supersonic shear flow

In this section we investigate shear velocities that are mildly supersonic also with respect to the hot layer. Figs 15 and 16 show series of snapshots for a shear flow of Mach number 1.5 relative to the hot layer and for different Re and for density contrasts 2 and 10, respectively. The 'hills' cool gas now cause bow shocks in the hot gas ahead of them. Because of the larger amount of momentum available for dissipation the viscous heating is more prominent at higher shear velocity and at higher viscosity. For all supersonic runs we smoothed the initial interface over 1 per cent of the perturbation length scale to suppress secondary instabilities and to avoid excessive viscous heating (see equation 14).

We applied the more interesting case of a Spitzer viscosity in Figs 15 and 16. At high Reynolds number, the KHI still evolves similar to the subsonic case. However, at such high velocities the compressibility of the gas affects the growth rate of the KHI and the classic estimate in equation (2) is not valid anymore (see review by Gerwin 1968 and references therein). One consequence is that in the 2D case a shear flow above a certain critical Mach number stabilizes the KHI. The case studied here is still below this limit. The viscous suppression of the KHI proceeds very similar to the subsonic case. At low density contrast (Fig. 15) the KHI is suppressed below Re $\lesssim$ 100, at a higher density contrast of 10 the critical Re is $\sim$30 (Fig. 16). The instability again enters the hybrid state where some vorticity is inserted in the cold layer.

5 DISCUSSION

We investigated the long-term evolution of the viscous KHI for the case of a constant kinematic viscosity and a strongly temperature-dependent Spitzer-like viscosity. We showed that viscosity suppresses the KHI below a critical Reynolds number and derived the dependence of this critical Reynolds number on density contrast, shear flow velocity and constant or temperature-dependent viscosity.

At high Reynolds numbers ($\gtrsim 10^4$) and moderate density contrasts ($\leq$10), our simulations reproduce the results of earlier inviscid KHI simulations and of the analytical estimate. Most of those

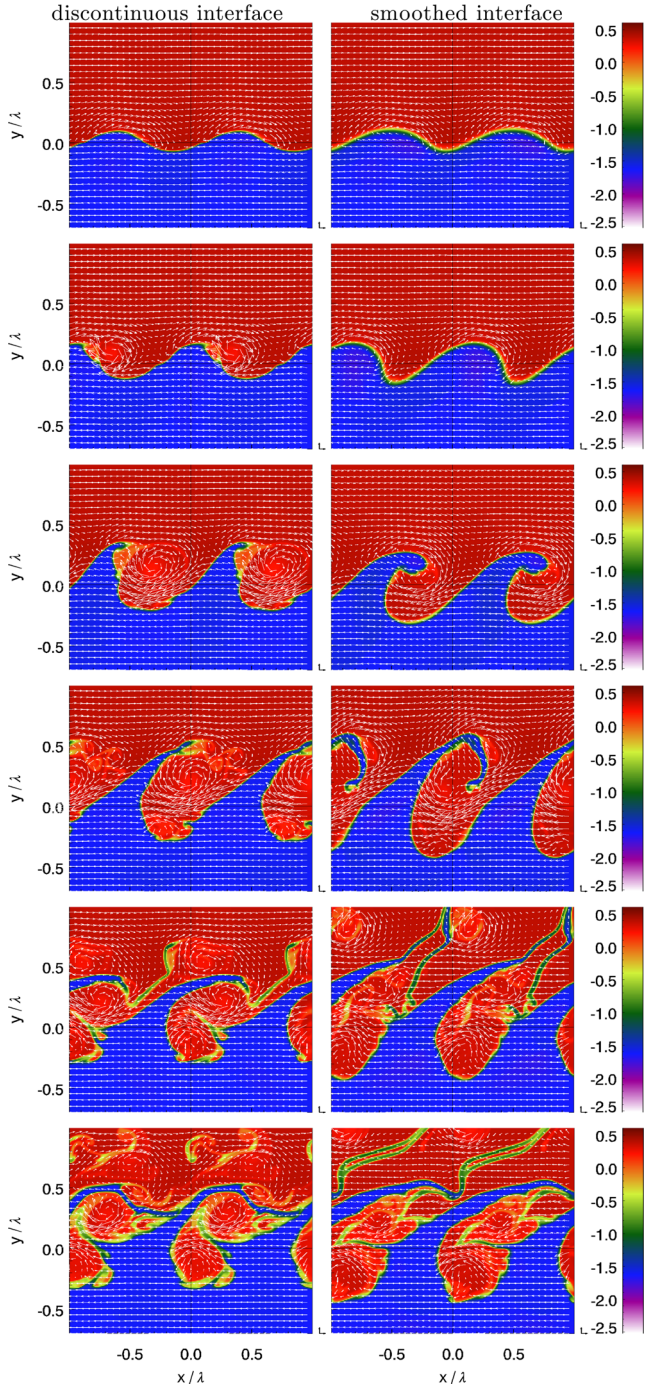

Figure 12. Snapshots for simulations with constant kinematic viscosity, density ratio of 100, shear flow Mach 0.5 and Reynolds number 10^4. The colour codes $\log(T/\mathrm{keV})$, velocity vectors are overlaid. The left-hand column has an initially discontinuous interface, in the right-hand column the interface is smoothed over 1/100 of the perturbation length. Rows from top to bottom are for time-steps 0.5, 1, 2, 3, 4, 5 τ_{KHinvisc}. The motion of the cold gas resembles 'growing mountains'. The hot gas is flowing over this distorted surface, developing turbulences. Hardly any turbulence is injected in the dense cold gas.

simulations, however, concentrate on the early phase of the KHI and use the numerically derived growth rate as a test for the code performance. Junk et al. (2010) presented viscous KHI simulations in order to determine the intrinsic viscosity of smoothed particle hydrodynamics (SPH) codes, and compared to viscous grid simulations with the FLASH code. They find a significantly weaker impact of viscosity than reported here. However, their analysis focuses on the onset of the instability only, i.e. long before the interface starts rolling up.

Our simulations were run in two dimensions, where modes with wave vectors inclined to the shear direction cannot exist. These can be the fastest growing modes for transonic shear speeds and the only unstable modes for supersonic shear (see Appendix A). However, the effect of viscosity is not expected to be significantly different in three dimensions because the viscous spreading of the shear flow discontinuity proceeds in the same manner. The reduction of the local shear velocity should affect all modes. The presence of the third dimension allows for more complex morphologies of the KH rolls. This effect, along with the influence of a realistic perturbation spectrum, is relevant for the detailed structure of the mixing layer, which will be the focus of a subsequent paper.

5.1 Plausible Reynolds numbers in the ICM

In the hydrodynamic paradigm, transport processes are related to the mean free path λ_{mfp} in the medium. For example, the dynamic viscosity is (Sarazin 1988)

$$\mu \approx \frac{1}{3}\rho c \lambda_{\mathrm{mfp}}, \tag{24}$$

where c the sound speed. In the hydrodynamic paradigm λ_{mfp} must be much smaller than scales of interest. This condition put limits on reasonable viscosities, or Reynolds numbers. For the KHI, we could demand that the mean free path is much smaller than the perturbation wavelength λ, say,

$$\lambda_{\mathrm{mfp}} < \lambda/10. \tag{25}$$

With equations (24) and (7) this condition corresponds to

$$\mathrm{Re} > 15\,\frac{\mathrm{Ma}}{0.5}, \tag{26}$$

where $\mathrm{Ma} = U/c$ is the Mach number of the shear velocity U. Thus, our derived critical Reynolds numbers are in the hydrodynamic regime where the required viscosity still implies a reasonable mean free path.

A second issue to consider is a possible saturation of viscosity, or more precisely, momentum transport. If the scale length of the velocity gradient is smaller than the mean free path, momentum transport as treated here becomes supersonic. As this is unrealistic, it would saturate to a maximum momentum flux (Sarazin 1988). Thus, for any given KHI set-up with shear velocity U, density ρ, perturbation wavelength λ and initial width of the interface w, we can rewrite the condition $w > \lambda_{\mathrm{mfp}}$ by using equation (24) to

$$\mathrm{Re}\,\frac{w}{\lambda} > 3\,\mathrm{Ma}, \tag{27}$$

thus expressing the minimal Reynolds number where viscosity can still act unsaturated. We note that $\mathrm{Re}\,w/\lambda = wU\rho/\mu = \mathrm{Re}_w$, the Reynolds number related to the initial width of the interface. We verified that an initial interface width of up to $w = 0.03\lambda$ influences the growth of the KHI only weakly. From $w = 0.1\lambda$ on the initial smoothing of the interface alone drastically slows down the KHI. Demanding $w \leq 0.03\lambda$, equation (27) requires $\mathrm{Re} > 100\,\mathrm{Ma}$ to remain in the unsaturated viscosity domain. At smaller Re, our simulations progressively overestimate the effect of viscosity. Consequently, our results for the constant kinematic viscosity are unaffected by the issue of saturation, because the KHI is already

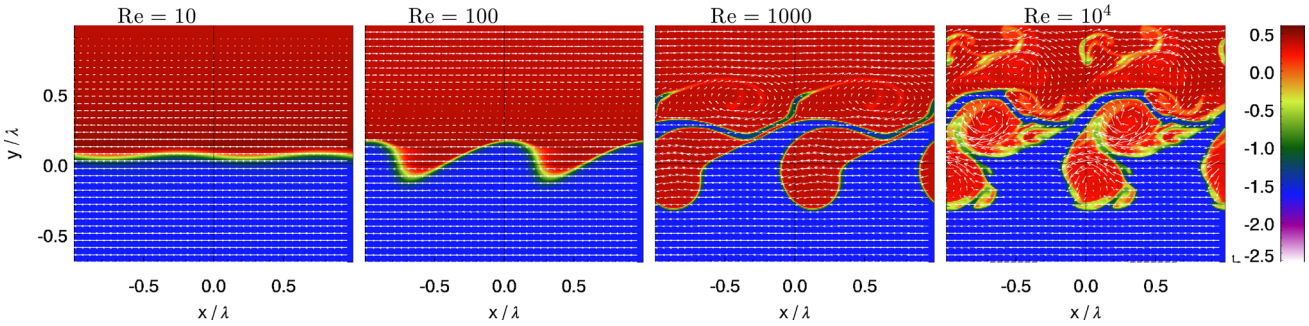

Figure 13. Snapshots for simulations with constant kinematic viscosity, a high density ratio of 100, shear flow of Mach 0.5 and different Re as given at the top. The colour codes $\log(T/\mathrm{keV})$, velocity vectors are overlaid. We show the time-step 5 τ_{KHinvisc}. Note the reversed flow direction in the hot layer near the interface for Re $\leq$ 100. For Re $\leq$ 100 we smoothed the initial interface over 1 per cent of the perturbation length scale to avoid excessive viscous heating at the shear flow discontinuity (see equation 14).

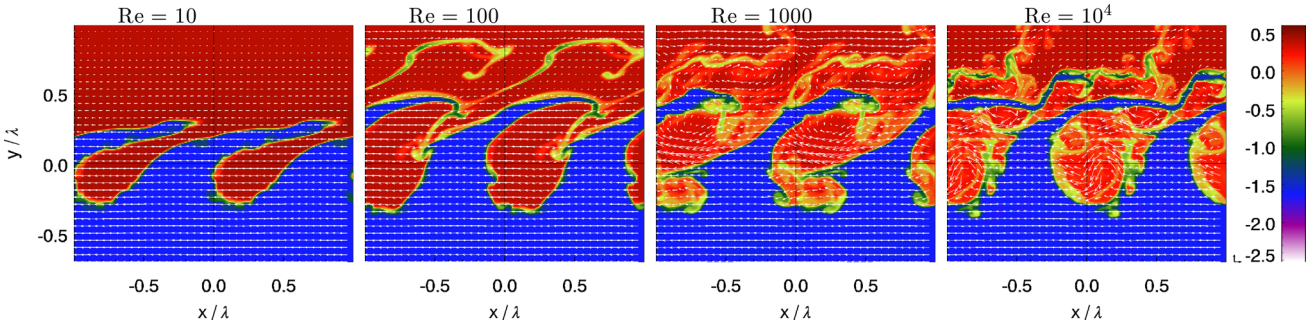

Figure 14. Same as Fig. 13 (density ratio of 100, shear flow of Mach 0.5), but with Spitzer viscosity. No smoothing of the initial interface is applied. Note the reversed flow direction in the hot layer near the interface for Re $\leq$ 100.

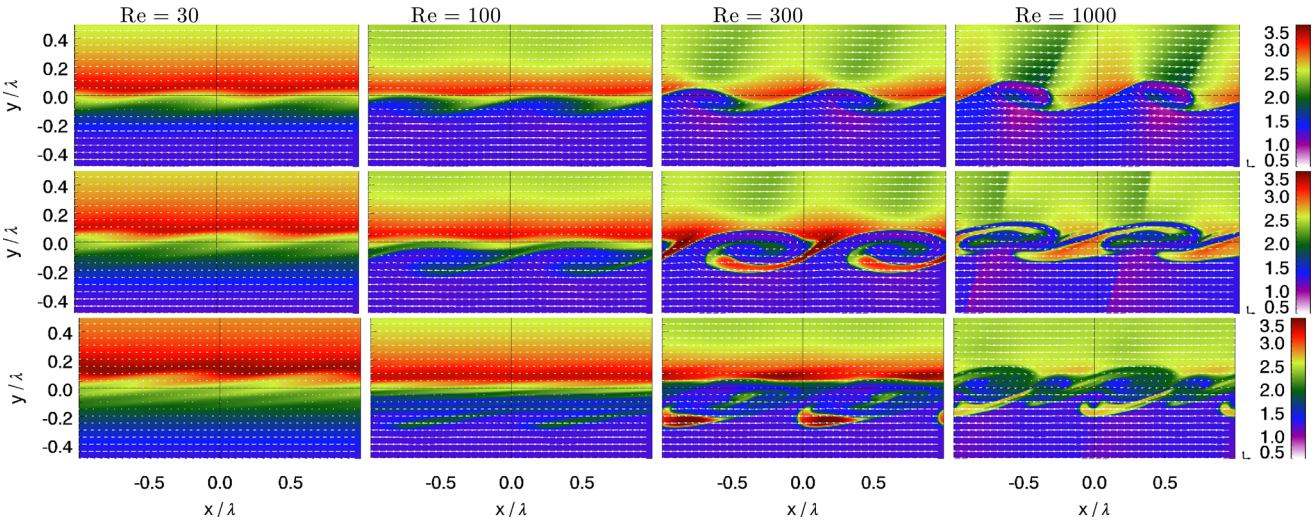

Figure 15. Snapshots for simulations with Spitzer viscosity, density ratio of 2, shear flow of Mach 1.5 (relative to hot layer) and different Re as given at the top. The colour codes T/keV, velocity vectors are overlaid. We show the time-steps 10, 20, 40 in units of τ_{KHinvisc}. We note that the comparison to the KHI growth time derived in equation (2) is only marginally meaningful, because this growth time assumes an incompressible gas, which is not true for supersonic flows.

suppressed for Re $\sim$ 100–200. In the case of a Spitzer-like viscosity Reynolds numbers of $\sim$30 are required to suppress the KHI even without taking saturation effects into account. This critical Re is only slightly below the saturation limit of equation (27), hence we conclude that also a Spitzer-like viscosity has a significant effect on the KHI. Given that the real behaviour of the ICM is even more complex than the question of saturated or unsaturated momentum transport, we refrain from investigating the details of a saturated momentum transport here.

We note that the nature of the effective viscosity in the ICM is still unclear, and the potentially large mean free path from Coulomb collisions may not even be a concern. For example, Guo et al. (2012) discuss in some detail the possible origin and amplitude of viscosity and conclude that Spitzer-like amplitude plausible.

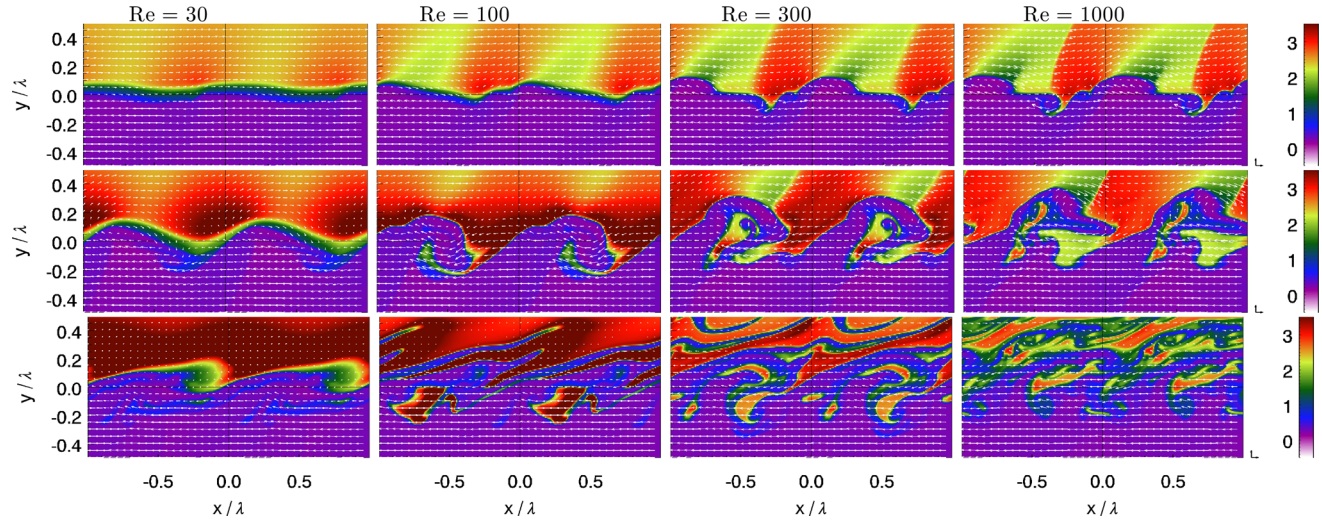

Figure 16. Snapshots for simulations with Spitzer viscosity, density ratio of 10, shear flow of Mach 1.5 (relative to hot layer) and different Re as given at the top. The colour codes T / keV, velocity vectors are overlaid. We show the time-steps 5, 10, 20 in units of $\tau_{\rm KHinvisc}$.

5.2 Application to specific shear layers

For any given shear layer, the condition for the growth of the KHI, $\mathrm{Re} > \mathrm{Re}_{\rm crit}$, can be translated into a critical wavelength above which the KHI can grow:

$$\lambda > \lambda_{\rm crit} = 30\,{\rm kpc}\,\frac{\mathrm{Re}_{\rm crit}}{30}\,f_\mu\,\left(\frac{U}{400\,{\rm km\,s^{-1}}}\right)^{-1} \times \left(\frac{n_{\rm e}}{10^{-3}\,{\rm cm^{-3}}}\right)^{-1}\,\left(\frac{kT_{\rm ICM}}{2.4\,{\rm keV}}\right)^{5/2}. \quad (28)$$

As a typical value, we used the more conservative $\mathrm{Re}_{\rm crit}$ for Spitzer-like viscosity here. We apply this relation to observed shear layers in the ICM in the following subsections.

5.2.1 *KHI at sloshing CFs*

In Roediger et al. (2012b) we applied a relation like equation (28) to sloshing CFs observed in several clusters and estimated whether or not these particular shear interfaces are expected to be KH unstable. In this work we used the too low critical Reynolds number based on the dispersion relation of Junk et al. (2010). Hence we update the estimates for $\lambda_{\rm crit}$ at these sloshing CFs with our improved, higher $\mathrm{Re}_{\rm crit}$ in Table 1. At full Spitzer viscosity, the KHI should be suppressed in the hottest cluster in this list, A2142, but KHIs could occur in cooler systems. Indeed, A496 and NGC 7618/UGC 12491 show characteristically distorted CFs.

The above estimate includes *solely* the effect of viscosity. Sloshing CFs, however, are special interfaces, and viscous suppression is not the only effect on KHIs here. The gas flow patterns at sloshing CFs lead to an enhanced temperature on the hotter side of the CFs by about a factor of 1.3 compared to the azimuthal average (see simulations; e.g. ZuHone, Markevitch & Johnson 2010; Roediger & ZuHone 2012), which boosts the effect of viscosity by a factor of ∼2 compared to the estimates given in Table 1. Additionally, modes above but close to the critical length scale are slowed down. Furthermore, gravity slows down or suppresses long modes even further. Finally, a sloshing CF itself, i.e. the shear interface, is a dynamic phenomenon and not a stationary interface. Thus, KHIs originating from a given perturbation have only a finite amount of time to grow into recognisable patterns. For example, at the northern CF in the Virgo cluster gravity suppresses KHI modes longer

Table 1. Full Spitzer viscosity should suppress the KHI for perturbations $<\lambda_{\rm crit}$ (equation 28). This table lists $\lambda_{\rm crit}$ at the sloshing CFs in different clusters, along with assumed values for temperature $T_{\rm ICM}$ and electron density $n_{\rm e}$ on the hotter side, and shear velocity U at each CF. Furthermore, we list for each CF its distance to the cluster/group centre $r_{\rm CF}$, and the scale of observed KHIs. Where no observed scale is given, the CF is not obviously distorted and a dedicated investigation is needed to determine upper limits on instability length scales.

Object	T (keV)	$n_{\rm e}$ (10^{-3} cm^{-3})	U (km s^{-1})	$\lambda_{\rm crit}$ (kpc)	$r_{\rm CF}$ (kpc)	Observed $\lambda_{\rm KHI}$ (kpc)
N7618/U12491[a]	1.2	2.5	200	4	20	15
Virgo[b] northern CF	2.5	2	300	22	90	
A496[c] northern CF	4.2	8	400	15	60	20
A2142[d] south-east CF	8	10	400	60	70	
A2142 north-west CF	8	2	600	200	360	

[a]Roediger et al. (2012b).
[b]Roediger et al. (2011).
[c]Roediger et al. (2012a).
[d]Markevitch et al. (2000).

than 50 kpc. Our Virgo-specific simulations (Roediger et al. 2013) demonstrate that, given the additional complexities of sloshing CFs, already 10 per cent of the Spitzer viscosity suppresses the KHI along the northern CF. Thus, in the context of sloshing CFs, the critical length scales given in Table 1 are lower limits only.

5.2.2 KHI at gas-stripped elliptical galaxies and subcluster merger cores

Galaxies moving through the ICM experience a ram pressure that can remove part of their interstellar medium (ISM), leading to a tail of stripped gas trailing behind the galaxy. Recent observations reveal the complex structure of such stripping tails for both spiral galaxies (Owers et al. 2012; Sun et al. (2010), Zhang et al., submitted) and elliptical galaxies (e.g. for the Virgo ellipticals M89, Machacek et al. (2006), Kraft et al., in prep., NGC 4472, Kraft et al. 2011, and M86, Randall et al. 2008, and the Fornax elliptical NGC 1404, Machacek et al. 2005). Churazov & Inogamov (2004) demonstrated that already a tiny intrinsic width of the interface between the galaxy gas and the ICM at the upstream side of such galaxies can suppress local KHIs. Consequently, KHIs appear only at the sides of the galaxy or along their tails, as confirmed by numerical simulations (e.g. Iapichino et al. 2008). These KHIs at the sides and the tail are a major agent to mix the cold stripped gas with the ambient ICM.

We applied equation (28) to several galaxies and calculated expected critical wavelengths for full Spitzer viscosity. The result, along with assumptions regarding shear flow and gas densities in the ICM, is listed in Table 2. For the Virgo ellipticals NGC 4552, NGC 4472 and M86, the critical perturbation length exceeds the current radius of the galaxies' ISM atmospheres by a factor of several, whereas for the Fornax elliptical NGC 1404 the radius of the gaseous halo and the critical length is comparable. Thus, at full Spitzer viscosity, none of the galaxies should experience KHIs at its sides, and the tails should start mixing with the ICM only several ISM radii downstream. If viscosity is suppressed at a comparable level in all cases, NGC 1404 is most likely to experience KHIs.

The observations of these galaxies draw a mixed picture. M86 has a spectacular cold and 150 kpc long tail, suggesting a significant suppression of mixing. NGC 4472 and NGC 4552 show distorted upstream edges resembling KHIs on scales smaller than the critical length scale. NGC 1404 has a smooth upstream edge, but a filamentary and warm tail.

The shear flows at gas-stripped elliptical galaxies are in the intermediate density contrast regime $2 < D_\rho < 10$. Depending on the nature of viscosity, the flow patterns may be particularly interesting. If viscosity is Spitzer like, the galaxy stripping can occur in the hybrid KHI regime where viscous damping suppresses the mixing of the cool gas stripped from the galaxy, but the cool stripped tail could be internally turbulent.

The cores of subclusters falling through their host clusters undergo a scenario very similar to the gas-stripped galaxies. We include in Table 2 the Bullet Cluster and A3667. In the former case, the small remnant merger core is surrounded by hot, shocked gas, and we expect KHIs only on scales much larger than the merger core. No obvious distortions in its upstream CF are observed. In contrast, the CF in A3667 shows kinks on scales of $\sim$200 kpc (see e.g. fig. 3 in Owers et al. 2009, also Mazzotta, Fusco-Femiano & Vikhlinin 2002). This is roughly consistent with our expected critical perturbation length of $\sim$300 kpc.

5.2.3 High-velocity clouds

High-velocity clouds (HVCs) falling into the haloes of the Milky Way or other galaxies are to some degree a scaled-down version of elliptical galaxies falling into clusters. While the HVCs themselves have a cold core of atomic gas, the galactic halo gas is an ionized plasma like the ICM. Indeed, at full Spitzer viscosity, the infall of HVCs leads to a similar low Reynolds number as for the galaxy stripping:

$$\mathrm{Re} = 7\, f_\mu^{-1} \left(\frac{V}{100\,\mathrm{km\,s^{-1}}}\right) \left(\frac{R}{0.1\,\mathrm{kpc}}\right) \times \left(\frac{n_\mathrm{e}}{10^{-4}\,\mathrm{cm^{-3}}}\right) \left(\frac{kT_\mathrm{ICM}}{0.1\,\mathrm{keV}}\right)^{-5/2}. \quad (29)$$

To our knowledge, HVCs have been studied only in the high Reynolds number regime (e.g. Heitsch & Putman 2009; Pittard, Hartquist & Falle 2010). The density contrasts between the cloud surface and the halo gas can be high, $\gtrsim$100, but we would expect a full Spitzer viscosity to have a stabilizing effect on instabilities at the

Table 2. Full Spitzer viscosity should suppress the KHI for perturbations $<\lambda_\mathrm{crit}$ (equation 28). This table lists the critical wavelength λ_crit for several gas-stripped elliptical galaxies and remnant merger cores, along with the assumed ambient ICM temperature T_ICM, ambient electron density n_e and galaxy infall velocity v_gal. We assume a shear velocity at the side of the galaxy/merger core of 0.5 v_gal. Furthermore, we list for each galaxy/merger core the radius of its current ISM atmosphere r_gas, and the scale of observed KHIs, λ_KHI.

Object	T_ICM (keV)	n_e (10^{-3} cm^{-3})	v_gal (km s^{-1})	λ_crit (kpc)	r_gas (kpc)	Observed λ_KHI (kpc)
NGC 4552 (M89)[a]	2.5	0.3	1700	50	3	3
NGC 4472 (M49)[b]	2–2.5	0.1–0.2	950–1500	50–270	20	10
M86[c]	2.5	0.2	1700	76	25	
NGC 1404[d]	1.5	1	600	12	8	
Bullet Cluster[e]	18	3	1350	440	20	
A3667[f]	8	0.8	700	420	300	200

[a]Machacek et al. (2006).
[b]Kraft et al. (2011).
[c]Randall et al. (2008).
[d]Machacek et al. (2005).
[e]Owers et al. (2009), Markevitch et al. (2002) and Springel & Farrar (2007).
[f]Owers et al. (2009) and Vikhlinin & Markevitch (2002).

cloud surface. The mixing between the stripped gas and the ambient halo gas is of particular interest as it can be traced in various ion lines (see Kwak, Henley & Shelton 2011, and references therein). As discussed by Kwak & Shelton (2010) and Kwak et al. (2011), the mixing and the interpretation of the observational data are complex due to additional effects like radiative cooling and non-equilibrium ionization. Our results indicate that even if the viscosity may not fully suppress KHIs at scales of the cloud radius, it could be relevant for the final mixing levels in the cloud tails, i.e. whether stripped and ambient gas truly mix or whether cold clumps can remain. In addition to viscosity, also thermal conduction (Vieser & Hensler 2007) and magnetic draping could be relevant for the evolution of HVCs.

5.2.4 AGN cavities

In inviscid simulations, buoyantly rising AGN inflated bubbles are disrupted by RTIs and KHIs. The simulations of Reynolds et al. (2005) and Guo et al. (2012) demonstrated that a viscosity below full Spitzer viscosity can stabilize both buoyantly rising cavities as well as recently inflated cavities. The density contrast between the gas exterior and interior of the simulated cavities is around 100. The AGN inflated cavities are thought to be filled with a relativistic plasma whose viscosity is unconstrained either. Both of the above simulations use a constant dynamic viscosity as a first approximation in studying the stability of the cavities. Reynolds et al. (2005) find viscosity stabilizes the buoyantly rising cavities for $\mathrm{Re} \lesssim 250$ ($\sim$1/4 Spitzer for their values), where their Reynolds number refers to the size of their cavities. The resolved KHIs that disrupt the cavities in their inviscid simulations are a factor of a few smaller than the bubble size, hence the Reynolds number for these dominant KHIs is of the order of 100 when they are suppressed. This agrees with our prediction.

Guo et al. (2012) simulated the impact of viscosity on the stability of the Fermi bubbles observed in our Galaxy. To this end, they simulate the inflation of such bubbles in a viscous galaxy halo gas by an AGN jet. Already for viscosities of 0.1–1 per cent of the Spitzer level, viscosity can prevent KHIs at the boundaries of the inflated bubbles. The lower level of viscosity compared to the Spitzer value is sufficient here because the bubble inflation causes shock heating of the ambient gas, where the higher temperature also boosts the viscosity. Given that their simulations cover the highly dynamic cavity inflation phase, also the critical Reynolds number will change with time. Using canonical values for their simulation of shear velocity of 1000 km s^{-1} at the bubble boundary, a density of 10^{-29} g cm^{-3} inside the bubble, 10^{-28} g cm^{-3} outside the bubble, a dynamic viscosity of 1 g cm^{-1} s^{-1} and perturbation length scale of 2 kpc, results in Reynolds numbers of 6 and 60 in the hot and cold layer, respectively. At this viscosity the KHI at the bubble boundary is significantly suppressed in Guo et al.'s simulations. Given the high density contrast and the dynamic context, this is in rough agreement with our estimate.

Dong & Stone (2009) investigate the interplay of anisotropic viscosity and magnetic field strength on rising cavities. They show that the evolution of the bubbles depends significantly on the field geometry. For example, horizontal magnetic fields lead to bubbles that are stabilized only along the direction of the field lines. They thus would appear coherent when seen along a line-of-sight perpendicular to the field lines, but disrupted otherwise. With toroidal fields the bubbles transform into a stable ring. The situation of tangled magnetic fields has not been studied.

5.2.5 Turbulence in the ICM

In hot clusters full Spitzer viscosity implies that important scales such as Kolmogorov scale $\eta \sim \frac{L}{\mathrm{Re}^{3/4}}$ or Taylor scale $\lambda_\mathrm{T} \sim \frac{3L}{\mathrm{Re}^{1/2}}$ may be resolvable with the current generation of X-ray observatories. Here L and Re are the integral scale the corresponding Reynolds number. For example, in the Coma Cluster core $T \approx 8.5$ keV, $n_\mathrm{e} \approx 410^{-3}$ cm^{-3}. Using Spitzer viscosity, the Mach number $\sim$0.25 and driving scale $L \sim 500$ kpc, yields $\eta \sim 20$ kpc and $\lambda_\mathrm{T} \sim 170$ kpc. The scales above $\sim$30 kpc can be probed via the surface brightness analysis (e.g. Churazov et al. 2012). The scales predicted by the equation (28) (for the velocity of 400 km s^{-1}) also fall into this range. In fact, numerically it is close to the Taylor scale λ. It will therefore be possible to search for structural changes in the density/velocity perturbation spectrum around these scales. It is interesting that in the recent simulations of the Coma Cluster (Gaspari & Churazov 2013) with the effective viscosity at the level comparable to the Spitzer value, the Mach number of $\sim$0.25 and the Reynolds number $\sim 10^2$, clear steepening of the density fluctuations power spectrum is indeed seen at scales of few tens of kpc.

6 SUMMARY

We investigated the long-term evolution of the viscous KHI for the case of a constant kinematic viscosity and a strongly temperature-dependent Spitzer-like viscosity. We considered density ratios between the shear flow layers from 1 to 100. We expressed our results in terms of the Reynolds number that relates to the perturbation scale, i.e. as defined in equation (7).

We showed that a constant kinematic viscosity suppresses the KHI for Reynolds numbers $\leq$100, and already for $\mathrm{Re} \leq 200$ for density contrasts $\lesssim$2. This agrees well with our analytic estimate of the critical Reynolds number at low density contrasts. We note that the long-term evolution of the boundary layer over 10 or 20 KHI growth times, i.e. the spinning of the KHI rolls, is affected already for Reynolds numbers of $\sim$1000. We derive an empirical relation between the viscous KHI growth time and Re (see equation 21 combined with equations 22 and 23).

The strong temperature dependence of the Spitzer viscosity causes a significant difference of Reynolds numbers between the hot and the cold layer in a shear flow. The ratio of Reynolds numbers scales as $D_\rho^{7/2}$. Consequently, only the viscosity in the hotter layer can suppress the instability, and Reynolds numbers below $\sim$30 or 10 are required for density contrast of 2 or $>$10, respectively. In fact, at intermediate density contrasts around 10 the KHI enters a hybrid state where it does not mix both fluids, but induces turbulence in the cold layer. At lower density contrasts the evolution becomes more symmetric between both layers.

At higher density contrast (at 100), the inertia of the cold dense layer is so large that turbulence is not induced in the cold layer even for high Reynolds numbers.

We apply our results to potential mixing layers in the ICM in galaxy clusters, i.e. sloshing CFs, gas-stripped galaxies, AGN cavities and turbulence. The difference between ongoing or suppressed mixing is observable with current X-ray observatories. There are several observations that indicate a viscosity significantly below the Spitzer value, but not all observations fit this picture straightforwardly. It may well be that additional ICM properties such as magnetic fields or anisotropic transport processes even on macroscopic scales are required to explain all observations consistently.

ACKNOWLEDGEMENTS

ER acknowledges the support of the Priority Programme 'Physics of the ISM' of the German Research Foundation (DFG), the supercomputing grants NIC 5027 and 6006 at the John-Neumann Institut at the Forschungszentrum Jülich and the hospitality of CfA during a Visiting Scientist Fellowship. We thank Fulai Guo and Robi Banerjee for helpful discussions.

REFERENCES

Amsden A. A., Harlow F. H., 1964, Phys. Fluids, 7, 327
Batchelor G. K., 2000, An Introduction to Fluid Dynamics, Cambridge edn. Cambridge Univ. Press, Cambridge
Bonafede A., Feretti L., Murgia M., Govoni F., Giovannini G., Dallacasa D., Dolag K., Taylor G. B., 2010, A&A, 513, A30
Chandrasekhar S., 1961, Hydrodynamic and Hydromagnetic Stability. Clarendon, Oxford
Churazov E., Inogamov N., 2004, MNRAS, 350, L52
Churazov E. et al., 2012, MNRAS, 421, 1123
Dong R., Stone J. M., 2009, ApJ, 704, 1309
Drazin P. G., Reid W. H., 2004, Hydrodynamic Stability, 2nd edn. Cambridge Univ. Press, Cambridge
Dubey A., Antypas K., Ganapathy M. K., Reid L. B., Riley K., Sheeler D., Siegel A., Weide K., 2009, Parallel Comput., 35, 512
Dupke R., White R. E., III, Bregman J. N., 2007, ApJ, 671, 181
Dursi L. J., Pfrommer C., 2008, ApJ, 677, 993
Esch R. E., 1957, J. Fluid Mech., 3, 289
Ferrari C., Govoni F., Schindler S., Bykov A. M., Rephaeli Y., 2008, Space Sci. Rev., 134, 93
Gaspari M., Churazov E., 2013, A&A, submitted (arXiv:1307.4397)
Gerwin R., 1968, Rev. Modern Phys., 40, 652
Guo F., Mathews W. G., Dobler G., Oh S. P., 2012, ApJ, 756, 182
Heitsch F., Putman M. E., 2009, ApJ, 698, 1485
Iapichino L., Adamek J., Schmidt W., Niemeyer J. C., 2008, MNRAS, 388, 1079
Junk V., Walch S., Heitsch F., Burkert A., Wetzstein M., Schartmann M., Price D., 2010, MNRAS, 407, 1933
Kaiser C. R., Pavlovski G., Pope E. C. D., Fangohr H., 2005, MNRAS, 359, 493
Kraft R. P. et al., 2011, ApJ, 727, 41
Kunz M. W., Bogdanović T., Reynolds C. S., Stone J. M., 2012, ApJ, 754, 122
Kwak K., Shelton R. L., 2010, ApJ, 719, 523
Kwak K., Henley D. B., Shelton R. L., 2011, ApJ, 739, 30
Lamb H., 1932, Hydrodynamics, 6th edn. Cambridge Univ. Press, Cambridge
Landau L. D., Lifschitz E. M., 1991, Lehrbuch der Theoretischen Physik. Akademie-Verlag, Berlin
Lyutikov M., 2006, MNRAS, 373, 73
Machacek M. E., Dosaj A., Forman W. R., Jones C., Markevitch M., Vikhlinin A., Warmflash A., Kraft R. P., 2005, ApJ, 621, 663
Machacek M. E., Jones C., Forman W. R., Nulsen P. E. J., 2006, ApJ, 644, 155
McNally C. P., Lyra W., Passy J.-C., 2012, ApJS, 201, 18
Markevitch M. et al., 2000, ApJ, 541, 542
Markevitch M., Gonzalez A. H., David L., Vikhlinin A., Murray S., Forman W. R., Jones C., Tucker W., 2002, ApJ, 567, L27
Mazzotta P., Fusco-Femiano R., Vikhlinin A., 2002, ApJ, 569, L31
Narayan R., Medvedev M. V., 2001, ApJ, 562, L129
Nulsen P. E. J., 1982, MNRAS, 198, 1007
Owers M. S., Nulsen P. E. J., Couch W. J., Markevitch M., 2009, ApJ, 704, 1349
Owers M. S., Couch W. J., Nulsen P. E. J., Randall S. W., 2012, ApJ, 750, L23
Pittard J. M., Hartquist T. W., Falle S. A. E. G., 2010, MNRAS, 405, 821
Randall S. W., Nulsen P. E. J., Forman W. R., Jones C., Machacek M. E., Murray S. S., Maughan B., 2008, ApJ, 688, 208
Reynolds C. S., McKernan B., Fabian A. C., Stone J. M., Vernaleo J. C., 2005, MNRAS, 357, 242
Roediger E., Brüggen M., 2008, MNRAS, 388, L89
Roediger E., ZuHone J. A., 2012, MNRAS, 419, 1338
Roediger E., Brüggen M., Simionescu A., Böhringer H., Churazov E., Forman W. R., 2011, MNRAS, 413, 2057
Roediger E., Lovisari L., Dupke R., Ghizzardi S., Brüggen M., Kraft R. P., Machacek M. E., 2012a, MNRAS, 420, 3632
Roediger E., Kraft R. P., Machacek M. E., Forman W. R., Nulsen P. E. J., Jones C., Murray S. S., 2012b, ApJ, 754, 147
Roediger E., Kraft R. P., Forman W. R., Nulsen P. E. J., Churazov E., 2013, ApJ, 764, 60
Rosin M. S., Schekochihin A. A., Rincon F., Cowley S. C., 2011, MNRAS, 413, 7
Ruszkowski M., Enßlin T. A., Brüggen M., Heinz S., Pfrommer C., 2007, MNRAS, 378, 662
Ruszkowski M., Bruggen M., Lee D., Shin M.-S., 2012, ApJ, submitted (arXiv:1203.1343)
Sarazin C. L., 1988, X-ray Emission from Clusters of Galaxies, Cambridge edn. Cambridge Univ. Press, Cambridge
Spitzer L., 1956, Physics of Fully Ionized Gases. Interscience Publishers, New York
Springel V., Farrar G. R., 2007, MNRAS, 380, 911
Sun M., Donahue M., Roediger E., Nulsen P. E. J., Voit G. M., Sarazin C., Forman W. R., Jones C., 2010, ApJ, 708, 946
Vieser W., Hensler G., 2007, A&A, 472, 141
Vikhlinin A. A., Markevitch M., 2002, Astron. Lett., 28, 495
Villermaux E., 1998, Phys. Fluids, 10, 368
ZuHone J. A., Markevitch M., Johnson R. E., 2010, ApJ, 717, 908
ZuHone J. A., Markevitch M., Lee D., 2011, ApJ, 743, 16

APPENDIX A: COMPRESSIBILITY

At shear speeds approaching the sound speed, compressibility alters the behaviour of the KHI. The dispersion relation for modes in a shear layer between two compressible fluids may be written as (Gerwin 1968; Nulsen 1982)

$$\left(\frac{\omega}{ks_\mathrm{h}}-\frac{k_x v_0}{ks_\mathrm{h}}\right)^2\left\{\left(\frac{\omega}{ks_\mathrm{h}}\right)^2-\left(\frac{s_\mathrm{c}}{s_\mathrm{h}}\right)^2\right\}-\left(\frac{\omega}{ks_\mathrm{h}}\right)^2=0, \quad \text{(A1)}$$

where v_0 is the shear speed, s_h is the sound speed in the hotter, lower density phase and s_c is the sound speed in the cooler phase. For gases of interest here, the density ratio is generally related to these by $D_\rho = s_\mathrm{h}^2/s_\mathrm{c}^2$ (although this is modified e.g. when the shearing layers are in different states). The wave vector is confined to the shear layer, but it need not be parallel to the shear direction. Its magnitude is k, while k_x is its component in the shear direction, so that $k_x v_0/(ks_\mathrm{h})$ is the Mach number in the hot phase of the shear velocity projected on to the wave vector. The complex frequency, ω, here is measured in a frame at rest with respect to the cooler phase. This quartic equation for ω always has two real roots. The remaining two roots are a complex conjugate pair, so that one corresponds to a growing mode, if

$$\frac{k_x v_0}{ks_\mathrm{h}} < \left\{1+\left(\frac{s_\mathrm{c}}{s_\mathrm{h}}\right)^{2/3}\right\}^{3/2}. \quad \text{(A2)}$$

Fig. A1 shows the real and imaginary parts of the scaled frequency, $\omega/(ks_\mathrm{h})$, plotted against the effective Mach number, $k_x v_0/(ks_\mathrm{h})$, for the case when $s_\mathrm{c}^2/s_\mathrm{h}^2 = 0.1$, corresponding to a density ratio of 10 (cf. Fig. 16). The full line shows the growth rate, i.e. the imaginary part of $\omega/(ks_\mathrm{h})$, while the dash–dot line shows

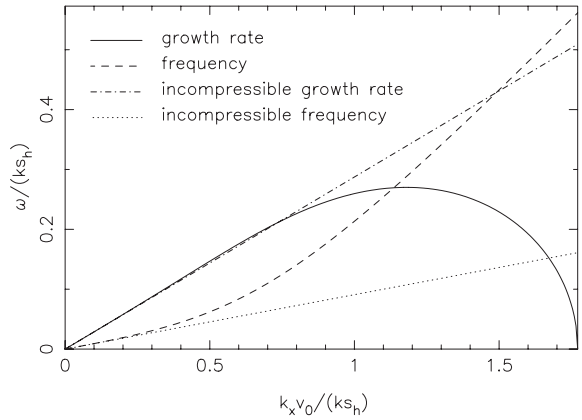

Figure A1. Real and imaginary parts of the frequency for unstable KHI modes in compressible fluids when $s_c^2/s_h^2 = 0.1$. As indicated in the legend, the curves show the real part (frequency) and imaginary part (growth rate) of the scale frequency, ω/ks_h, for the growing KHI modes in a shear layer of speed v_0. The independent variable, $k_x v_0/(ks_h)$, gives the Mach number measured in the hotter fluid of the shear velocity projected on to the wave vector of a mode.

the same thing for the incompressible case. The dashed line shows the real part of $\omega/(ks_h)$ and the dotted line shows the same thing for the incompressible case. As expected, the incompressible approximation is good for low Mach numbers, but fails as the effective Mach number approaches unity. For effective Mach numbers $k_x v_0/(ks_h) \gtrsim 1.77$ in this case there are no growing modes. However, for larger Mach numbers, inclined modes with $k_x < k$ can still grow. Note also that for a Mach number of 1.5 (Section 4.5), the growth rate of the parallel mode with $k_x = k$ is slower than for inclined modes with $k_x v_0/(ks_h) \simeq 1.2$. Such modes are excluded in our 2D simulations, so we may have underestimated the true growth rate in this one case. It is the only case we have simulated where inclined modes may make an appreciable difference to the outcome.

APPENDIX B: CODE TESTS

We tested the viscosity implementation on two set-ups with analytic solutions.

B1 Viscous flow between plates

We set up the classic viscous flow between two plates, i.e. through a 2D pipe. Initially, the fluid has a homogeneous density and zero velocity. A constant pressure gradient is applied in x-direction. Boundary conditions are no-slip, i.e. $v_x = 0$, at the y-boundaries, and open in x-direction. The pressure gradient accelerates the fluid. Viscous forces lead to a parabolic profile in $v_x(y)$:

$$v_x(y) = v_{\max}\left(y^2 - d^2\right) \quad \text{with} \tag{B1}$$

$$v_{\max} = \frac{1}{2\nu\rho}\frac{\partial p}{\partial x}, \tag{B2}$$

where d is half the distance between the plates, ν the kinematic viscosity, ρ the gas density and $\partial p/\partial x$ the pressure gradient. Our chosen parameters (pipe diameter 10 kpc, maximum flow velocity 17.3 km s^{-1} and kinematic viscosity $\nu = 10^{29}$ cm^2 s^{-1}) correspond

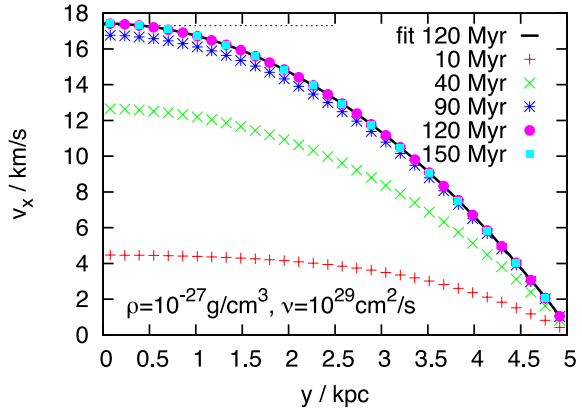

Figure B1. Viscous flow through a 2D pipe – profile of velocity component parallel to the pipe v_x as a function of position perpendicular to the pipe, y. The centre of the pipe is at $y = 0$, the outer boundaries are at $y = \pm 5$ kpc. Symbols of different colour denote different time-steps. As the flow started from zero velocity, some time is needed to reach the predicted steady state. The black line is the fit of the analytic prediction (equation B1) to the simulation result, leaving the viscosity as a free parameter. We recover the viscosity within 1 or 2 per cent.

to a Reynolds number of 0.5. We ran the same test for a 30 times higher Re. The pipe is sufficiently long such that at its centre in x-direction a steady state is reached before boundary effects reach the centre. Fig. B1 shows velocity profiles $v_x(y)$ at different time-steps. We measure the actual viscosity in the simulation by fitting equation (B1) to the final time-step, leaving the viscosity as a free parameter. We recover the intended viscosity within 1 or 2 per cent.

B2 Viscous smoothing of a shear flow discontinuity

We set up the same shear box like in our KHI tests, but induce no perturbation. Because of momentum diffusion, viscosity spreads the initial discontinuity in horizontal velocity $v_x(y)$, according to

$$v_x(y) = \mathrm{erf}\left(\frac{y}{2\sqrt{\nu t}}\right). \tag{B3}$$

This behaviour is shown in Fig. B2. Symbols denote simulation results. For each time-step, we fit the simulation results with the expected analytical function (lines in Fig. B2), leaving the viscosity as a free parameter. We recover the intended viscosity within 1 per cent.

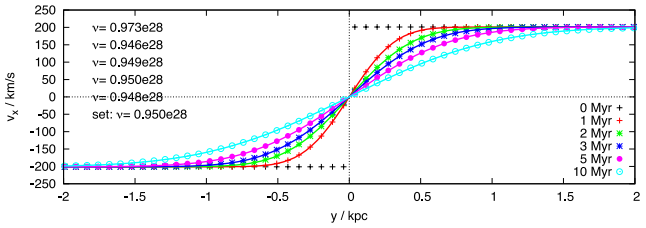

Figure B2. Viscous smoothing of shear flow discontinuity. Initially, v_x has a discontinuity in y-direction, which is progressively smoothed out by viscosity. Symbols denote simulation results, colours and symbol styles code different times. Lines of matching colour present fits of the analytic prediction (equation B3) to the simulation results. The viscosity is left as a free parameter. The fit results and the originally set viscosity are listed on the left.

APPENDIX C: ANALYSIS METHODS

C1 Height of KH rolls

We measure the height of the KH rolls, or the width of the KH mixing interface, by using the fluid tracer F. Initially, F is set to 1 below the initial interface, and to 0 above the interface. In Fig. 1 we mark the 'edges' of the upper and lower fluid by the two thin black lines: for each x we find the maximum $y_{\rm up}(x)$ for gas with $F > 0.9$ and the minimum $y_{\rm down}(x)$ of gas with $F < 0.1$. We define the upwards height of the KH rolls as $h_{\rm up} = \max(y_{\rm up}(x))$, and the downwards height as $h_{\rm down} = \min(y_{\rm down}(x))$. In the case of equal densities as shown in Figs 1 and 2, the KHI evolves symmetrically and $h_{\rm up} = h_{\rm down}$. For unequal densities the KHI evolves asymmetrical, see Figs 7 and 10.

C2 Measuring KH growth times

We measure the growth time of the KHI by tracking the evolution of the maximum and minimum velocity in y-direction, $v_{\rm ymax}$ and $v_{\rm ymin}$. We note that these are not the velocity of the interface itself, but reflect also the spin-up of the KH rolls as demonstrated in the left-hand column in Fig. 1. This simple method has the potential risk of contamination by noise-seeded, unintentional secondary KHIs. Many previous works used Fourier filtering to bypass this problem. We find that the presence of at least a small amount of viscosity avoids secondary instabilities in most of our simulations. For example, in Fig. 1 even at a Reynolds number of 1000 only the intended instability exists. At still higher Re, we slightly smooth the initial interface (see equation 14), which mostly avoids the secondary instabilities. Only in the equal density case does the KHI evolve symmetrically. For all other cases we follow the minimum and maximum v_y separately.

For sufficiently high Re, $v_{\rm ymax}$ and $v_{\rm ymin}$ show an initial exponential increase which reflects the growth of the KHI (except for very high density contrasts, see Section 4.4). We fit this initial increase with an exponential function

$$v_{\rm max/min}(t) = v_0 \exp(t/\tau_{\rm KHvisc}) \quad \text{(C1)}$$

with free amplitude v_0 and growth time $\tau_{\rm KHvisc}$. The latter is the derived viscous growth time. Examples for the fits are shown in Fig. 3. In all other corresponding plots, we only state the derived growth times for both directions, but do not plot the fitted function to avoid confusion. At low Re we can perform a similar fit during

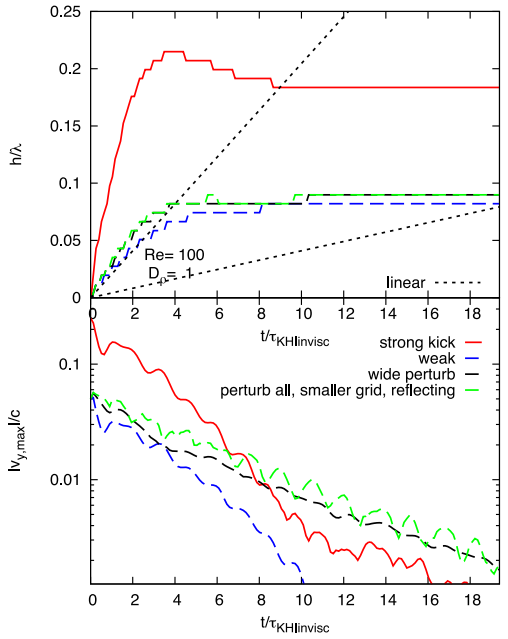

Figure D1. Impact of perturbation strength and region width. A higher initial perturbation does not help the instability to grow, neither does a wider perturbation layer around the interface. These simulations are for a constant kinematic viscosity, a density contrast of 1, a shear velocity of Mach 0.5 and a Reynolds number of 100.

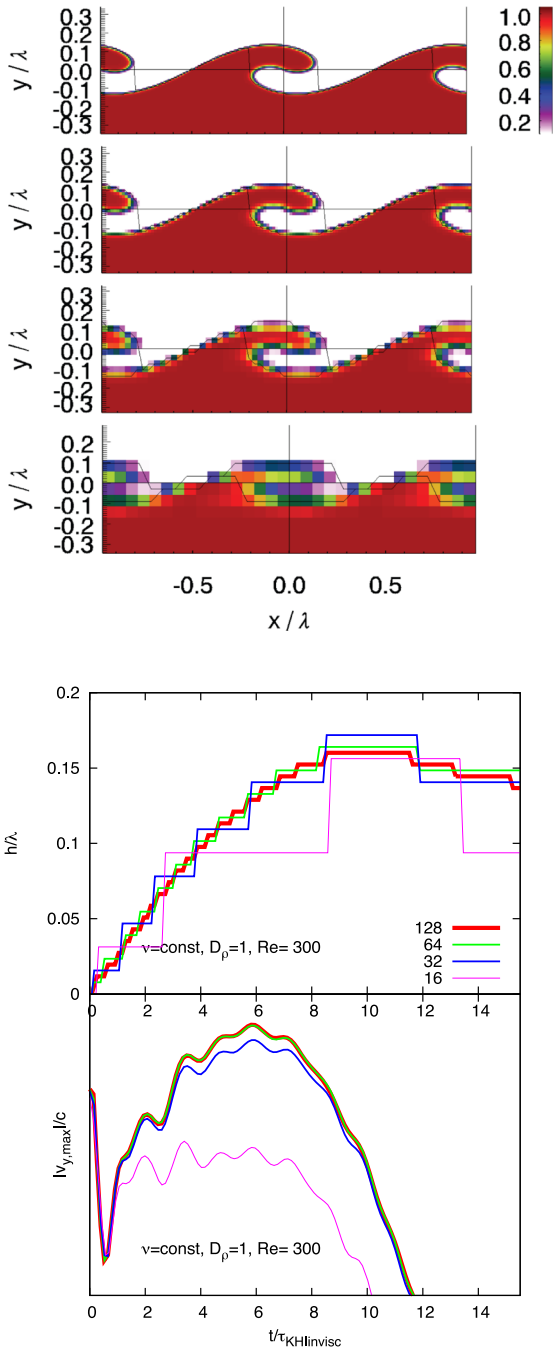

Figure E1. Resolution test: comparison of tracer slices for constant kinematic viscosity, density ratio 1, Reynolds number 300, shear flow Mach 0.5 and time-step 50 Myr $= 6.5\tau_{\rm KHinvisc}$. Top to bottom is 128, 64, 32, 16 cells per perturbation wavelength. The bottom line plot compares the height of the KHI rolls and the maximum vertical velocity.

the corresponding early evolution time. This results, however, in negative growth times, i.e. a suppressed instability.

APPENDIX D: IMPACT OF PERTURBATION STRENGTH AND REGION

We verify that our simulations do not overpredict the viscous damping of the KHI due to an insufficient perturbation. Fig. D1 demonstrates that neither a perturbation of much higher velocity amplitude nor a wider perturbation region can revive the KHI. We tested a perturbation velocity of half the shear velocity, and a perturbation scale width of 10 kpc instead of the standard 3 kpc. We also tested perturbing throughout the simulation grid, using reflecting boundaries at ± 10 kpc above and below the interface in this case. The viscous damping of the KHI is a robust result.

APPENDIX E: RESOLUTION TEST

In realistic contexts like gas stripping from galaxies or clouds, or cluster and galaxy mergers, the KHI is just one of several processes and is resolved with only tens of grid cells per wavelength or less, but not >100 grid cells as in idealized KHI tests. Therefore we test not only the convergence of our results, but also the ability of the FLASH code to capture the KHI with low resolution.

We compare tracer slices, the height of the KHI rolls and $v_{\rm ymax}$ for different resolutions in Fig. E1. The height of the KHI rolls is captured correctly for a resolution as low as 16 grid cells per perturbation length. We note that in this low resolution the height of the KH rolls above and below the original interface is only ± 2 grid cells. The morphology of the KH rolls is captured well down to resolutions of 32 cells per perturbation wavelength. The same is true for the evolution of $v_{\rm ymax}$. The peak $v_{\rm ymax}$ is about 10 per cent smaller than for the higher resolutions, but the initial increase and later decline are reproduced accurately. With only 16 grid cells per perturbation length, however, the scales on which the peak velocities occur are not resolved, and the growth rate would be underestimated. This is not surprising given that the thickness of the mixing layer is covered by only 4 grid cells.

The PPM hydro scheme spreads discontinuities over 2–3 grid cells as evident from the tracer slices in Fig. E1. Consequently, the internal structure of the KH rolls requires resolutions of the *width* of the KH layer exceeding several grid cells. For example, the intermediate tracer values in the KH rolls at the lowest resolution are due only to numerical diffusion. The low resolution results resemble the higher resolution results well except for this caveat.

This paper has been typeset from a TEX/LATEX file prepared by the author.